Journal Pre-proof

Benchmark of a probabilistic fatigue software based on machined and as-built components manufactured in AlSi10Mg by L-PBF

F. Sausto, S. Romano, L. Patriarca, S. Miccoli, S. Beretta

PII: S0142-1123(22)00425-X
DOI: https://doi.org/10.1016/j.ijfatigue.2022.107171
Reference: JIJF 107171

To appear in: *International Journal of Fatigue*

Received date : 4 March 2022
Revised date : 23 July 2022
Accepted date : 25 July 2022

Please cite this article as: F. Sausto, S. Romano, L. Patriarca et al., Benchmark of a probabilistic fatigue software based on machined and as-built components manufactured in AlSi10Mg by L-PBF. *International Journal of Fatigue* (2022), doi: https://doi.org/10.1016/j.ijfatigue.2022.107171.

Benchmark of a probabilistic fatigue software based on machined and as-built components manufactured in AlSi10Mg by L-PBF

F. Sausto[a], S. Romano[b], L. Patriarca[a], S. Miccoli[a], S. Beretta[a,*]

[a] *Department of Mechanical Engineering, Politecnico di Milano, via La Masa 1, 20156, Milano (MI), Italy*
[b] *Department of Mechanical Engineering, Politecnico di Milano, via La Masa 1, 20156, Milano (MI), Italy. Now GE Avio s.r.l., Via Primo Maggio 99, 10040, Rivalta di Torino (TO), Italy*

Abstract

The possibility to obtain optimized components with a reduced weight is the main driver of space and aeronautic industries in seriously considering the metal additive manufacturing (AM) technology for production. Despite the incontrovertible advantages offered by this manufacturing technique, the material produced is usually affected by the presence of internal defects, a poor surface quality, and process-induced residual stresses. These features strongly affect the fatigue performance and reproducibility of AMed parts, limiting the adoption of deterministic criteria for fatigue assessment. A probabilistic approach is therefore needed for the analysis of critical and structural components. To this aim, a fully probabilistic finite element (FE) post-processor, ProFACE, was developed by part of the authors to assess the fatigue strength and critical locations of complex components in the presence of process-induced defects. A wide benchmark activity was supported by the European Space Agency (ESA) to test the software capabilities for the life prediction of components manufactured in AlSi10Mg by L-PBF. After tuning ProFACE parameters based on the results obtained on standard fatigue specimens, the software was used to estimate the fatigue life of the components obtaining a good description of the experimental dataset for both volumetric and surface defects. The software was then used to explore the effect of the variability of the most significant parameters affecting fatigue strength of AlSi10Mg AMed components.

Keywords: Additive manufacturing, fatigue, defects, as-built surface, failure probability, residual stresses.

*Corresponding author
Email address: stefano.beretta@polimi.it (S. Beretta)

Nomenclature

a	crack depth
B	inverted slope of the SN curve
N_f	number of cycles to failure
$N_{k,\sigma}$	knee point of the SN curve
P_{f}	failure probability
$P_{\mathrm{f,norm}}$	normalized failure probability
$P_{\mathrm{f,target}}$	target failure probability
$\mathcal{R}_i$	reliability of the i-th element of the chain, referred to volume or surface
R	stress ratio
R_{eff}	effective stress range
R_L	load ratio
Y	Murakami's boundary correction factor
δ	scale parameter of the LEVD
λ	location parameter of the LEVD
$\Delta K_{\mathrm{th,lc}}$	fatigue crack threshold
ΔS	applied stress range
$\Delta\sigma_{\mathrm{w}}$	fatigue stress range limit with respect to the material defectology
$\Delta\sigma_{\mathrm{w},0}$	fatigue stress range limit for defect-free material
σ_{RS}	measured residual stress
$\sqrt{\mathrm{area}}$	square root of the defect area
$\sqrt{\mathrm{area}}_0$	El-Haddad parameter
$\sqrt{\mathrm{area}}_{\mathrm{cr}}$	critical defect's square root area

Abbreviations

AM	additive manufacturing
AMed	additively manufactured
cdf	cumulative density function
CIFS	critical initial flaw size
CT	computed tomography
DT	damage tolerance
EC	eddy current
ESA	European Space Agency
FCG	fatigue crack growth
FE	finite element
F-N	force range versus the number of cycles to failure curve
GEV	generalised extreme value distribution
HCF	high cycle fatigue
HIP	hot isostatic processing
LEVD	largest extreme values distribution
LF	loading factor
L-PBF	laser powder bed fusion
MTC	Manufacturing Technology Centre
NDE	non-destructive evaluation
PDT	probabilistic damage tolerant
PoD	probability of detection
PT	penetrant testing
SEM	scanning electron microscope

SIF	stress intensity factor
S-N	stress range versus the number of cycles to failure curve
UTS	ultimate tensile stress
XRD	X-ray diffraction

1. Introduction

Metal additive manufacturing (AM) is nowadays considered a full-fledged technology taken into consideration for many industrial applications. In the recent years, most companies have switched from building demonstrators to actual production, and the number of AM parts currently in service has sensibly increased. In fact, most of the largest aerospace, automotive, and biomedical industries have now developed internal design practices and acceptability standards based on years of lessons learnt, growing process control capabilities, and huge amount of data collected and analyzed. For aerospace parts, the development of such know-how is expected to bring an increase of AM part criticality as this technology matures and gains widespread acceptance [1]. Despite this, the number of AM applications of critical or structural parts remains very limited. This is mostly due to insufficient regulatory framework for qualification and certification. Due to the high focus on quality coupled with low production volumes and strive for mass reduction, the space industry is leading the effort for closing this gap and space regulators are continuing the development of enabling standards and methods [2, 3]. At the same time, additional standardization efforts are ongoing, driven by other organizations among which ASTM and ISO [4, 5].

The main challenges of AM technology with respect to other legacy manufacturing methods are mostly related to damage tolerance and fracture control for mitigating catastrophic hazards resulting from the growth of an unknown pre-existing crack-like defect [6]. In fact, AM structural parts are prone to fatigue failure originated from anomalies despite several improvements are being introduced in the latest AM machines, e.g., sensors integration, which allows for a more robust implementation of in-situ monitoring and process control methodologies [7, 8, 9]. Therefore, a defect tolerant design becomes of primary importance at level of design and component qualification.

As a general statement, anomaly types can be subdivided in two categories: process anomalies and material anomalies. The first class refers to those process-induced anomalies which cause evident quality issues, e.g., build stop, build line skipped, cracking or deformation caused by residual stresses during cooling. On one hand, it is fundamental that the anomalies falling in this class are always avoided in service. In general, this can be obtained via non-destructive evaluation (NDE) and in-situ monitoring. On the other hand, the occurrence of such defects is usually minimized by the presence of a consolidated process, part production plan, and process simulation. Material anomalies due to AM processes can be further distinguished in volumetric or surface. The first category comprehends all those anomalies that can occur anywhere in the build, e.g., keyhole porosity, lack of fusion, inclusions [10, 11, 12]. Several works have been performed to model the effects of volumetric defects on fatigue based on fracture mechanics models [12, 13, 14, 15, 16] in which crack growth rate and thresholds account for the *short crack effect* (i.e., they are dependent on defect size). As for surface anomalies, this category comprehends all those anomalies that can occur only in the presence of a free surface, e.g., surface microcracks and protrusions, localised stresses caused by coarse surface roughness, or porosity placed below the outer skin. Also for these surface features a number of papers have shown the applicability of fracture-based approaches [16, 17, 18, 19, 20, 21, 22, 23, 24, 25, 26].

1.1. Probabilistic damage tolerance approaches

Due to the random nature of material anomalies (not specific to AM materials), the FAA Advisory Circular 33.70-1 defining damage tolerance requirements for engine life limited parts states that "the probabilistic approach to damage tolerance assessment is one of two elements necessary to appropriately assess damage tolerance" [27]. In this regard, the most simple semi-probabilistic approach is the standard option for damage tolerance assessments in which the initial flaw size is conservatively assumed considering that the part contains the largest anomalies that the NDE can miss with a 90 % probability of detection (PoD) and 95 % confidence. The assessment is then performed adopting a minimum safety factor $\eta = 4$ for the service life [28, 29].

The upper level of probabilistic analysis is to consider a *fully probabilistic approach*. The recent draft document by NASA [3] reports a *complete* probabilistic damage tolerant (PDT) analysis as an acceptable mean of compliance for fracture control of critical parts. To support such an assessment, an appropriate characterization of material anomalies is needed for developing the size distribution and frequency of occurrence of material anomalies. As discussed in [1], this information can be used to define an exceedance curve for a given class of material defects, which is the key input for probabilistic fracture mechanics-based assessments such as the one defined in the FAA Advisory Circulars 33.14-1 [30] and 33.70-2 [31] for specific types of material or manufacturing defects. In probabilistic terms, this input anomaly exceedance curve can be defined by inverting the PoD capability of the NDE methods adopted [3]. However, it should be noted that this procedure has two main drawbacks: (i) the level of conservatism might be, in some cases, excessive; (ii) multiple NDE techniques are usually necessary to cover all the possible surface and volumetric anomaly types, and the determination of a robust PoD for a generic geometry might become extremely challenging and expensive.

The second alternative available is deriving an exceedance curve based on the real anomaly distribution. It is interesting to highlight that the determination of an anomaly distribution for hard-alpha grains in titanium disks required years of collaboration by certification agencies, major aircraft engine manufacturers, and steel companies. On the other hand, characterizing anomalies in AM materials can be substantially easier due to the higher occurrence of anomalies, relatively low cost of in-house specimens production, and exploitation of more advanced NDE as X-ray micro computed tomography (CT) [10, 32, 33, 34, 35]. Once the anomaly distribution is known, statistical means can be successfully adopted to infer the critical defect size for larger volumes [10, 11, 36, 35]. Despite this approach might well cover the verification of actual build quality with respect to a qualified target for the selected AM machine and process (e.g., by analysis of witness samples [37]), the question remains if the distribution in the samples can cover the intrinsic variability of a complex component geometry when a detailed micro-CT characterization on the full part is not achievable. NASA draft [3] requires cut-ups on a sacrificial part to ensure that possible feature-dependent manufacturing issues are not present or covered by analysis. Such an approach would allow characterizing anomaly distributions in selected areas (e.g., highly stressed or complex to manufacture regions) with the aim of verifying buy-in with the qualified process curve or obtaining a more conservative anomaly exceedance

curve option to be used for PDT analysis of the specific regions of interest.

Besides material anomalies, other sources of variability affect the fatigue resistance of AMed materials. Residual stresses, microstructural variations, and anisotropy are other important factors that should be accounted in the fatigue assessment [12, 38, 39, 40, 41]. Among these variables, residual stresses are considered one of the weakest points in the component assessment due to their uncertainty/variability [12]. Recent results [17, 42] for the fatigue strength of as-built surfaces in AlSi10Mg show that residual stresses play a role as important as surface features at the fracture origin. In this regard, the probabilistic approach is possibly the best suited to account for so many sources of variability without the excessive conservatism that would be caused by classical deterministic approaches based on safety factors.

Many different approaches are available in the literature for probabilistic assessment based on a FE structural analysis and the presence of defects/anomalies: i) approaches based on weakest-link concepts and the underlying assumption of Weibull distributions [43, 44, 45]; ii) weakest-link approach based on a fatigue model combined with *extreme value* statistics for defects [46]; iii) explicit crack-growth simulations combined with Monte Carlo simulations [47, 48, 49, 50, 51, 52]. The weakest-link approaches have the advantage of implicit analytical formulations that drastically reduce the computational time, while the explicit crack growth simulations can precisely describe the life from the local stress field and they can be combined with analyses of defect detectability [53].

The real challenge is to apply these approaches using as an input the test campaign for process qualification and the data available from the component tests [2], so that they could become a support to design and qualification of components.

1.2. Scope of the paper

This is the topic of the research activity presented in this paper, where we discuss the application of *ProFACE* (**Pro**babilistic **F**atigue **A**ssessment of engineering **C**omponents with d**E**fects), a tool developed by Politecnico di Milano for the fatigue assessment of AMed components [46]. Figure 1 shows the schematic of ProFACE with the indications of the inputs/outputs and the methods. The basic inputs of the software (that is a post-processor of FE analyses) are the *process signature*, expressed by the distribution of defects and surface features due to the AM process and a suitable probabilistic model for fatigue strength in presence of defects (modelled as short cracks). The failure probabilities of the finite elements are then calculated with an approach based on *extreme value statistics* and then combined through a weakest-link model.

The upgraded ProFACE 2.0 version (including surface features and residual stresses) was tested in the framework of a benchmark activity funded by ESA, in which special demonstrators were printed and tested in the machined and as-built surface states, along with fatigue coupons aimed at calibrating the material properties and establish the anomaly distributions [54]. This paper is structured as follows:

- Section 2: the test campaign aimed at generating a set of fatigue data on specimens and on a specially designed benchmark component;

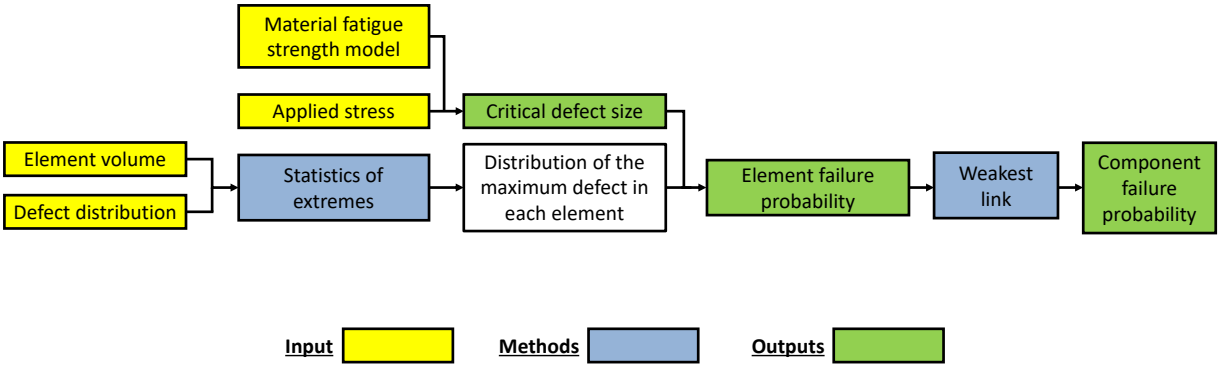

Figure 1: Schematic of the computational flow of ProFACE.

- Section 3: the new features of the software, with its capabilities to handle the presence of residual stresses and the distribution of superficial features associated to the as-built surface state;
- Section 4: application of ProFACE to the ESA benchmark campaign by analysing specimens and components;
- Section 5: a sensitivity analysis on the two most significant variables, i.e., the residual stresses and anomaly distributions.

2. Benchmark experimental database

This section summarizes the experimental results obtained in the framework of a benchmark activity between ESA, the Manufacturing Technology Center (MTC, Coventry) and Politecnico di Milano [54]. This benchmark activity was aimed at preparing an experimental database for validating fracture-based fatigue assessments and probabilistic analyses through the ProFACE software. Duties for the benchmark campaign were the following: MTC was in charge of project management, specimen and component manufacturing; Politecnico di Milano was in charge of tests on specimens, life prediction models and analysis with ProFACE; ESA performed X-ray diffraction (XRD) measurements, fatigue tests and roughness measurements on benchmark components. More details on all activities, along with the experimental database, are extensively described in [54]. The test results are presented here for the sake of: i) providing input data for ProFACE analyses; ii) allowing for comparison of predictions with real experimental data.

2.1. Test pieces and test campaign

The benchmark activity employed fatigue specimens and benchmark components, see Figure 2, that were manufactured by L-PBF in AlSi10Mg. No thermal treatment was carried out on test pieces after 3D printing. The benchmark components (in the following named as wishbones) were designed by PoliMi in order to manufacture a relatively simple part (similar to isostatic mounting devices adopted in space industry) featuring a competition of three critical locations, to reproduce the condition of multiple fatigue critical regions in optimised AM components. Details of the stress state in the critical locations are given in [54].

A cylindrical specimen geometry (diameter of 6 mm) was adopted for the determination of the S-N diagram for both machined and as-built conditions (Figure 2.a), with a shape compliant to ASTM E466 [55] standard. A total of 23 specimens were manufactured and successively tested in the as-built condition, while other 17 specimens were used to characterise the machined condition. The specimens were produced from three different AM builds together with the benchmark components, whose geometry is depicted in Figure 2.b.

Among the 30 benchmark components manufactured, one half was tested in the as-built condition, while the second half was tested after surface machining. Machined wishbones were printed with a material overstock to allow that both machined and as-built parts had the same nominal dimensions. Other specimen geometries were also manufactured to measure the crack growth rates (single edge bending specimens) and the tensile behaviour. More details on test specimens and test conditions are reported in [54].

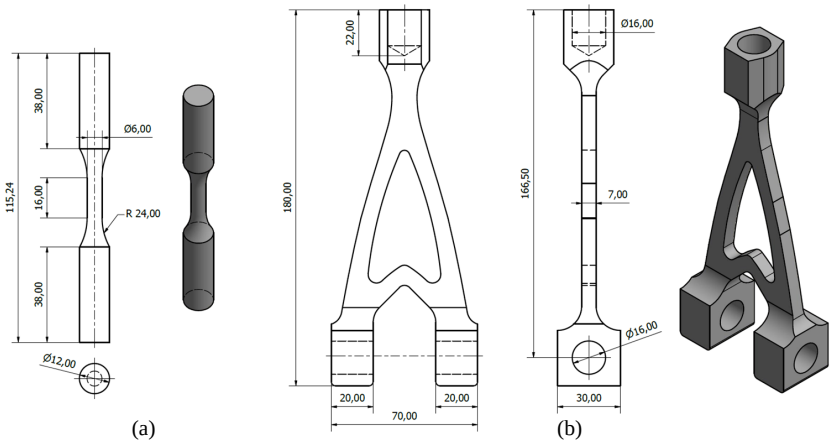

Figure 2: Specimens tested: a) cylindrical specimens and b) benchmark component.

Table 1: Mean AlSi10Mg tensile properties obtained from the tensile tests [54].

Property	Mean
Ultimate Tensile Stress	469 MPa
Yield Stress	258 MPa
Elastic Modulus	69.5 GPa
Elongation at fracture	8.34 %

2.2. Residual stress measurements

The residual stresses were measured on the fatigue specimens by means of an AST X-Stress 3000 portable X-ray diffractometer using the $\sin^2\psi$ method. The measurements were taken in the mid axial length and repeated in four symmetric positions along the circumference. The stress component parallel to the loading direction was considered and reported in Table 2 together with its deviation. The machined specimens displayed compressive stresses, while the as-built specimens were characterised by tensile stresses.

Table 2: Results of the measurement of the residual stress for the cylindrical fatigue specimens.

Condition	σ_{RS} [MPa]	Deviation [MPa]
Machined	-76	-9
As-built	60	15

The residual stresses of the wishbone demonstrators were measured by means of a Bruker D8 Discover diffractometer equipped with VANTEC-500 area detector with a Cu-Kα radiation at 40 kV, 50 µm and a 1 mm collimator size. The magnitude and sign were seen to differ depending on the position on the wishbone demonstrators and on the surface condition (machined versus as-built). A summary of the measurements

performed on the wishbone demonstrators is provided in Table 3. Compressive residual stresses were measured on the front surface ($\sigma_{\mathrm{RS}}^{\mathrm{front}}$) of the machined wishbone demonstrators (first view in Figure 2.b), while tensile stresses were found on the lateral surfaces $\sigma_{\mathrm{RS}}^{\mathrm{side}}$ (second view in Figure 2.b). As for the as-built wishbone demonstrators, all residual stresses were measured to be in tension. A comprehensive database of all the residual stress measurements performed can be found in [54].

Table 3: Results of the residual stress measurements performed on the wishbones.

Condition	$\sigma_{\mathrm{RS}}^{\mathrm{front}}$ [MPa]	Deviation$^{\mathrm{front}}$ [MPa]	$\sigma_{\mathrm{RS}}^{\mathrm{side}}$ [MPa]	Deviation$^{\mathrm{side}}$ [MPa]
Machined	-100	23.5	60	30
As-built	60	10.9	60	10.9

2.3. Uniaxial fatigue of standard specimens

Figure 3 shows the S-N curves obtained from the cylindrical machined and as-built specimens. The tests were conducted in laod-control at load ratio of $R_L = 0.1$ under a uniaxial Instron ElectroPuls E10000 machine equipped with a 10 kN load cell.

The run-out condition was set at 5×10^6 cycles, however one test for each condition was also extended until 1×10^7 cycles. The equation $N = A \cdot \Delta S^B$ was used to fit the data points corresponding to failures according to the least square method (ASTM-E739 standard [56]), while the Dixon up and down method was used to calculate the endurance limits [57]. The experimental data-points were fitted with a three parameters Gaussian distribution considering a constant standard deviation $\sigma_{\log N}$; the parameters obtained are reported in Table 4. The S-N curves showed that the as-built condition is detrimental to the fatigue performance, in particular the endurance limit was observed to decrease from $\Delta\sigma_{\mathrm{w}} = 152$ MPa to 48 MPa.

Reference [54] contains all the images of the fracture surfaces captured by the scanning electron microscope (SEM). The analyses of the fracture surfaces highlighted the features that originated the failures. Small pores and defects were observed near the surfaces of machined specimens. These defects remained after the surface's machining and were characterised by equal depth and length. Oppositely, the failures of the as-built specimens were triggered by shallow surface defects represented by the typical features observed on as-built surfaces of AlSi10Mg manufactured by L-PBF.

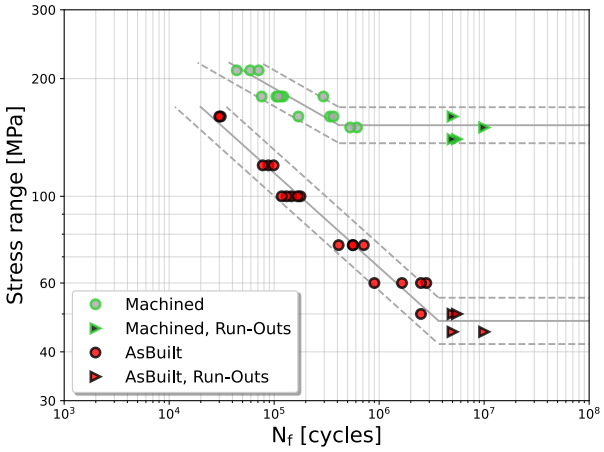

Figure 3: Results of the fatigue tests of the uniaxial cylindrical specimens [54].

Table 4: Summary of the fitting constants of the S-N curves shown in Figure 3.

Condition	A	B	$\sigma_{\log N}$	$\sigma_{\log S}$
Machined	19.9	-6.54	0.1537	0.0235
As-built	13.53	-4.09	0.1251	0.0302

2.4. Benchmark component fatigue results

The tests performed on the benchmark components were conducted on two different machines depending on the maximum load of the test: i) an Instron ElectroPuls E10000 machine equipped with a 10 kN load cell; ii) a servo-hydraulic fatigue testing system Instron 8802 equipped with a 250 kN load cell. As for the cylindrical fatigue specimens, the tests were conducted at a load ratio of $R_L = 0.1$, while the frequency ranged between 9 Hz and 20 Hz, depending on the test machine used. The run-out condition was set to 1×10^7 cycles. A complete break of the wishbone was considered as the test failure condition. The benchmark components that did not show any evident damage after the fatigue test were successively re-tested at higher loads to populate the force range versus the number of cycles to failure (F-N) curves and reveal the killer defect.

The F-N curves of the benchmark components are reported in Figure 4.a. Four load levels were selected in the finite life region for the as-built condition and three for the machined condition. Figure 4.b indicates the points of maximum stress according a static finite element (FE) analysis [54]. Accordingly, the F-N curves were corroborated with the point of failure for all the tests. The failure positions are also summarised in Table 5. The data shown indicate that the majority of failures occurred at the location P2 for the machined condition, while the location that occurred more frequently was P3 for the as-built condition.

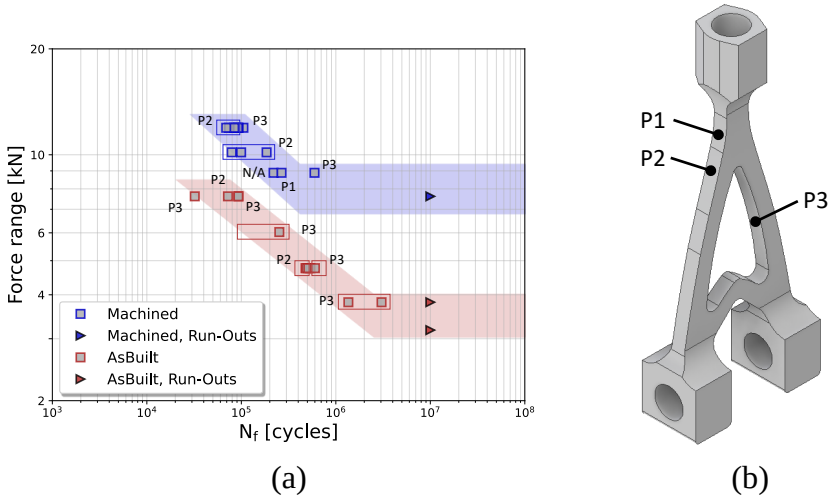

Figure 4: Fatigue results and failure locations of the wishbones: a) machined and as-built wishbones' results and b) schematic of the failure locations [54].

Table 5: Number of failures for the critical locations of the benchmark components as indicated in Figure 4 [54].

	Number of failures		
Benchmark component	**Location P1**	**Location P2**	**Location P3**
Machined	1	9	2
As-built	0	3	10

2.5. Analysis of defects

The dimension of defects at the fracture origin of the standard laboratory specimens can generally be statistically described with the largest extreme value distribution (LEVD) whose cumulative density function has the expression reported in Equation (1):

$$F_{\mathrm{LEVD}}(x) = \exp\left[-\exp\left(-\frac{x-\lambda}{\delta}\right)\right] \tag{1}$$

where x is the defect size, λ is the location (i.e. the 36.8-*th* percentile) and δ the scale parameters. Moving from the standard specimens to a load-bearing component, the fatigue strength decreases; this phenomenon is known as *scaling effect* [58] and it is linked with a higher probability of finding a large defect inside a material volume which is bigger than the one of the standard specimens. The defect distributions that caused the final failure of machined and as-built wishbones are shown in Figure 5.a and Figure 5.b respectively, while the fitted parameters are reported in Table 6. These two distributions are not fully consistent with those found in fatigue specimens, showing a larger average defect for the benchmark components. This is consistent for with larger component material volume (and surface). To properly account for this scaling effect in the fatigue analysis, a statistical-based approach is required.

The two techniques for handling this effect in terms of failure probability for a given material volume, namely a FE volume, are: i) a weakest-link approach where the failure probability is calculated for any defect in a material volume and the material volume is considered a *series system*; ii) an *extreme value* approach in which the failure probability is calculated for the maximum defect occurring in the material volume. It can be demonstrated that the two approaches are equivalent [59]. ProFACE adopts the latter approach for calculating the failure probability of FEs.

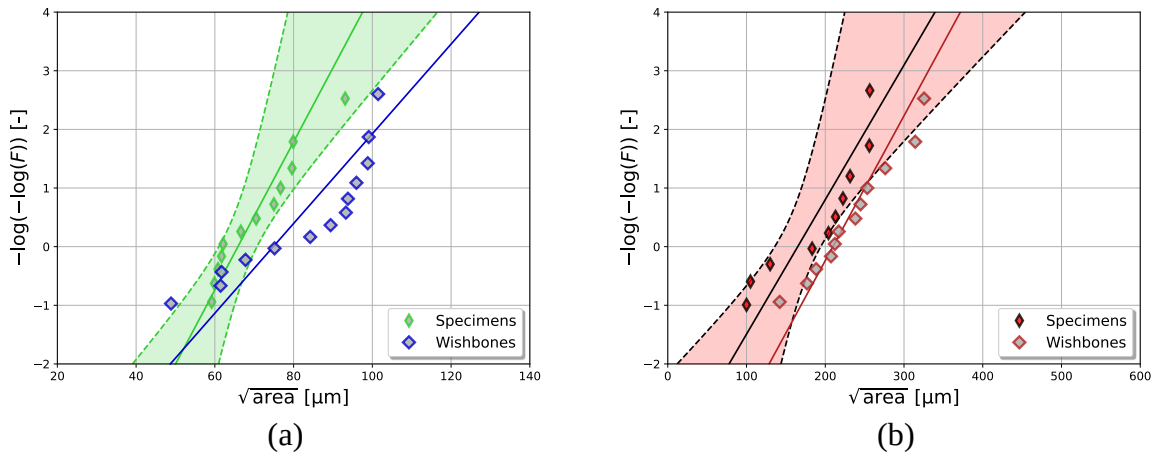

Figure 5: Comparison of the LEVD defect distributions: a) machined specimens and wishbones and b) as-built specimens and wishbones.

Table 6: LEVD parameters of the machined and as-built specimens and wishbones with the relative errors on the estimators.

Type	λ [µm]	λ_{up} [µm]	λ_{lo} [µm]	δ [µm]	δ_{up} [µm]	δ_{lo} [µm]
Machined surface						
Specimens	65.9	69.0	62.7	7.9	11.7	5.4
Wishbones	74.8	79.9	69.8	13.1	19.0	9.0
As-built surface						
Specimens	165.0	194.2	135.8	43.6	83.5	22.8
Wishbones	209.6	234.4	184.9	40.5	73.3	22.4

2.6. Fracture-based life predictions

As it happens in most of the optimised load-bearing components, the benchmark components are featured with multiple locations of similar criticality from which a crack can nucleate and propagate. As shown in Section 2.4, three critical locations were found in this experimental campaign (Figure 4, [54]). For each location, a deterministic life prediction was implemented considering fatigue crack growth calculations based on

the average killer defect (Figure 6.a from [54]), local stress distributions from FE analyses, and experimental residual stress profiles. In detail, the crack growth model was based on the NASGRO propagation equation and a suitable description of the *short-crack effect* (see Section 3 for details).

The comparison with the experimental results confirms that the approach based on fracture mechanics concepts can be successfully adopted for the life prediction of both the fatigue specimens and benchmark components. However, we have to remark that fatigue crack growth calculations are accurate only when all the variables considered (killer defect distribution, crack location, residual stresses) can be properly measured or assessed, as in the case of the fatigue specimens and benchmark components in [54].

The limitation of this deterministic approach is evident when considering that multiple prospective crack locations exist in the component, as well as variability in the key parameters (defect size, residual stress distributions), and different material volumes which are subjected to the scaling effect. Even considering the variability of life predictions at a single component region (as schematically reported in Figure 6.b), it would be impossible to implement the crack growth analyses for the entire component.

This limitation further supports the application of a probabilistic approach and the application of the ProFACE software [46] for its capabilities to predict the fatigue performance of wishbones from the input data obtained on specimens.

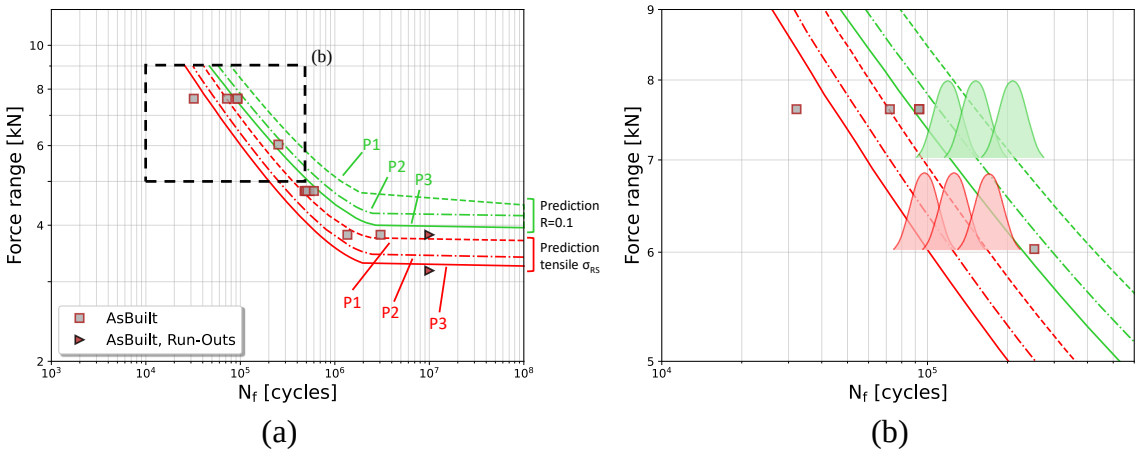

Figure 6: Results of the FCG propagation with NASGRO model of the critical locations against the experimental results: a) as-built benchmark components (from [54]) and b) scheme of the statistical variability of each as-built components location.

3. ProFACE: inputs and models

The backbone of ProFACE is the weakest-link model, based on which the component is considered as a chain of small sub-parts, each connected to the others with their own failure probability. According to this model, the loaded component fails if one element of the chain fails. The ingredients required to implement this approach are a fatigue strength model which links the stress associated with each sub-part with the dimension of the critical defect (a_{cr}), and a suitable defect distribution. The aim of this section is to describe the main fatigue and statistical models at the base of ProFACE, considering the common case in which the material is affected by the presence of residual stresses and featured with a rough external surface.

3.1. Fatigue model for defective materials

The common approach in the technical literature to link the fatigue strength with a known defect size is the adoption of the Kitagawa-Takahashi diagram, that can be described with the El-Haddad model [60]. This model can be extended to the finite fatigue life regime considering that the S-N curve, at the fatigue limit, coincides with the Kitagawa diagram as shown in [13, 46, 61]. The main hypothesis of the formulation proposed in [46] to compute the critical defect size $\sqrt{\mathrm{area}}_{\mathrm{cr}}$ is that the material manifests a fatigue limit below which no failure can happen. Actually some structural materials, including aluminium, do not display a marked endurance strength, showing instead a S-N curve characterised by two slopes in the region before and after the knee point $N_{k,\sigma}$. A value of 22 for the S-N curve's slope k_σ^* after the knee point $N_{k,\sigma}$ regime was fitted for the AMed AlSi10Mg alloy to describe the experimental data in [13], which is in line with that found in [62, 63]. In view of this fatigue behaviour of the AlSi10Mg alloy, the method to compute the critical defect in ProFACE was modified as:

$$\sqrt{\mathrm{area}}_{\mathrm{cr}} = \sqrt{\mathrm{area}}_0 \cdot \left\{ \left[\left(\frac{N_{k,\sigma}}{N_f} \right)^{1/B} \cdot \frac{\Delta\sigma_{\mathrm{w0}}}{\Delta \mathrm{S}} \right]^2 - 1 \right\} \qquad \text{with } B = \begin{cases} k_\sigma & N_f \leq N_{k,\sigma} \\ k_\sigma^* & N_f > N_{k,\sigma} \end{cases} \tag{2}$$

where $\Delta\sigma_{\mathrm{w},0}$ is the fatigue limit of the defect-free material, ΔS the applied stress range, N_f the number of cycles to failure, and B the inverted slope of the S-N curve in the two fatigue regimes. The parameter $\sqrt{\mathrm{area}}_0$ represents the boundary between long and short cracks, adopting an El-Haddad model [13], it can be computed through Equation (3):

$$\sqrt{\mathrm{area}}_0 = \frac{1}{\pi} \cdot \left(\frac{\Delta K_{\mathrm{th,lc}}}{Y \cdot \Delta\sigma_{\mathrm{w0}}} \right)^2 \tag{3}$$

where $\Delta K_{\mathrm{th,lc}}$ is the fatigue threshold for long cracks and Y the shape factor for irregular cracks, which is equal to 0.65 for superficial defects and 0.5 for volumetric ones.

The size of the critical defect $\sqrt{\mathrm{area}}_{\mathrm{cr}}$ depends on the effective stress ratio R_{eff} that results from the superposition of the mechanical and residual stresses. This can be modeled considering a Kitagawa diagram dependent on stress ratio. The dependence of $\Delta\sigma_{\mathrm{w0}}$ (fatigue limit of smooth specimens) can be obtained from tests or simple engineering models to describe the Haigh diagram [64, 65]. The dependence of the fatigue

threshold for long cracks on the stress ratio is instead modelled with the NASGRO equation, which can be fitted on experimental fatigue threshold tests or imported from databases. Details of the parameters of the fatigue strength model adopted for the AlSi10Mg are available in [54]. It is of some importance to remark that both the slope k_σ and the knee point $N_{k,\sigma}$ of the S-N curve in the HCF regime may also depend on the values of effective stress ratio [17, 66].

A schematic representation of the normalized S-N curve for the AlSi10Mg considered in this work at the reference load ratio of 0.1 is reported in Figure 7.a, while the Kitagawa diagrams obtained with Equation (2) at various number of cycles to failure are shown in Figure 7.b. Slightly different crack growth models [67, 68, 69] provide similar maps, as well as crack growth analyses based on ΔJ [70]. Equation (2) or maps $\Delta S = f\left(\sqrt{\text{area}}, N_f, R\right)$ enable the calculation of the *critical defect size* a_{cr} at any location for a given combination $(\Delta S, N_f, R)$ (see Equation 4 Subsection 3.2.1).

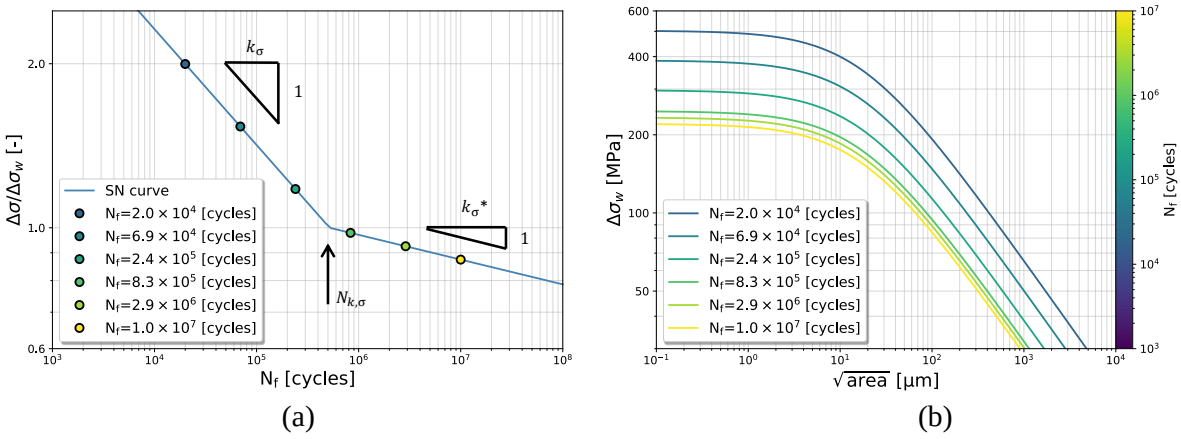

Figure 7: Schematic of the finite fatigue life model adopted in ProFACE for a general stress ratio $R = 0.1$: a) normalized S-N curve and b) generalised Kitagawa curves as a function of the number of cycles to failure.

Considering the 50 % percentile of the LEVD of the killer defects for the machined and as-built specimens in Table 6, Equation (2) can be inverted to compute the stress range versus the number of cycles to failure. These curves, which depend on the effective stress ratio, were obtained for the tested specimens and compared with the experimental data in Figure 8.a and Figure 8.b for machined and as-built specimens, respectively. The effective S-N curves overlap with the experimental data. One important remark is that the maximum stress of the fatigue cycle plus the tensile residual stress was higher than the yield limit for the maximum load level investigated. This determines the local elastic shake down that might completely relax the residual stress field. This effect is not considered in the calculation, and can thus be the reason for the distance between the experimental data and the computed mean S-N curve for the high stress range region of Figure 8.b (as-built specimens).

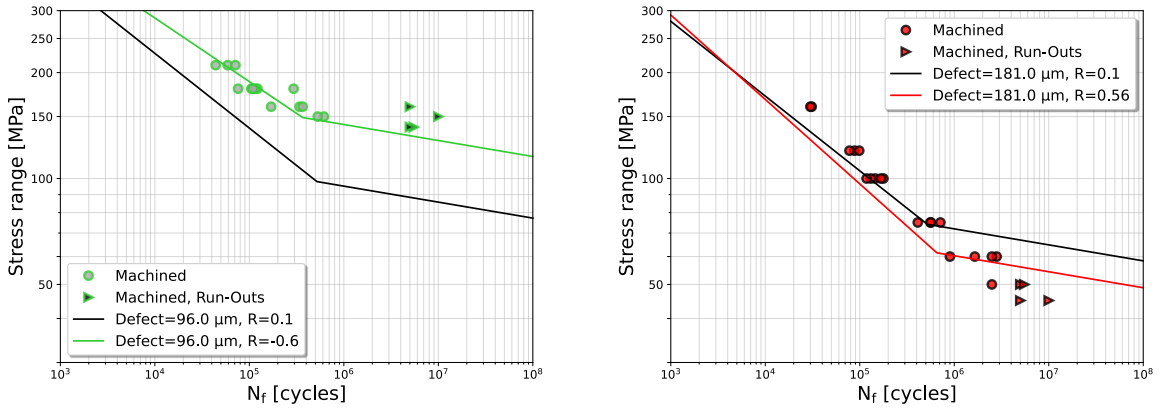

Figure 8: Comparison between the finite fatigue model with the experimental results of the cylindrical specimens: a) machined cylindrical specimens and b) as-built cylindrical specimens.

3.2. Input random variables

The two key ingredients of ProFACE probabilistic model are: i) the distribution of defects/inhomogeneities due to manufacturing process (volumetric defects and surface features) that can randomly occur in the material; ii) the inherent dispersion of the strength model represented by the Kitagawa diagram.

3.2.1. Defects and size effect

As for the defect distribution, the ProFACE's algorithm adopts an approach based on the *statistics of extremes* in which the reliability for a given volume V_i (or the i-th finite element) can be calculated as:

$$\mathcal{R}_{i,V_i} = \left[F_{a_{\max,V_i}}\left(a_{\mathrm{cr}}\right)\right] \tag{4}$$

where a_{cr} is the critical defect size for a stress and number of cycles calculated according to Equation (2) and $F_{a_{\max,V_i}}$ is the distribution of the maximum defect over V_i that can be conveniently described with different methods [58]. This approach inherently describes the size effect because $a_{\max,V_i}$ increases with the material volume. In fact, if we consider the distribution of the maximum defect $a_{\max}$ for two material volumes V_1 and V_2:

$$F(a_{\max,V_2}) = \left[F(a_{\max,V_1})\right]^{V_2/V_1} \tag{5}$$

where F is the generic cumulative density function (cdf) of the maximum defect distribution over a certain volume. This transformation, which is the base of *extreme value statistics*, is also the key ingredient of ProFACE in combination with Equation (4). The software adopts this approach, instead of assuming a given distribution for the fatigue strength (see [44, 45, 71]), because it allows us to consider any suitable *physically-based* threshold model (dependent on defect size) and to properly describe the distribution of maximum defect in a given reference volume V_0 [11, 58, 72].

It has been shown that the effect of the roughness in net-shape AM parts can be treated as an equivalent elongated superficial defect [17, 66, 73]. In the new implementation of ProFACE, the same concept presented for volumetric anomalies is applied to surface defects, whose distribution on two prospective areas S_1 and S_2 could be described as:

$$F(a_{\max,S_2}) = \left[F(a_{\max,S_1})\right]^{S_2/S_1} \tag{6}$$

Applying this transformation to the collected surface defects detected on specimens and wishbones, it could be seen that the experimental data-points were correctly described with equivalent negative exponential distributions considering the most stressed area (Figure 9.a). The software allows the user to describe the distribution of defects considering different options: LEVD, generalised extreme value distribution (GEV), and mixed distributions for data sampled with *block maxima*; log-normal, negative-exponential, and Weibull for data described in terms of *parent distribution* or *Peak Over Threshold* maxima sampling.

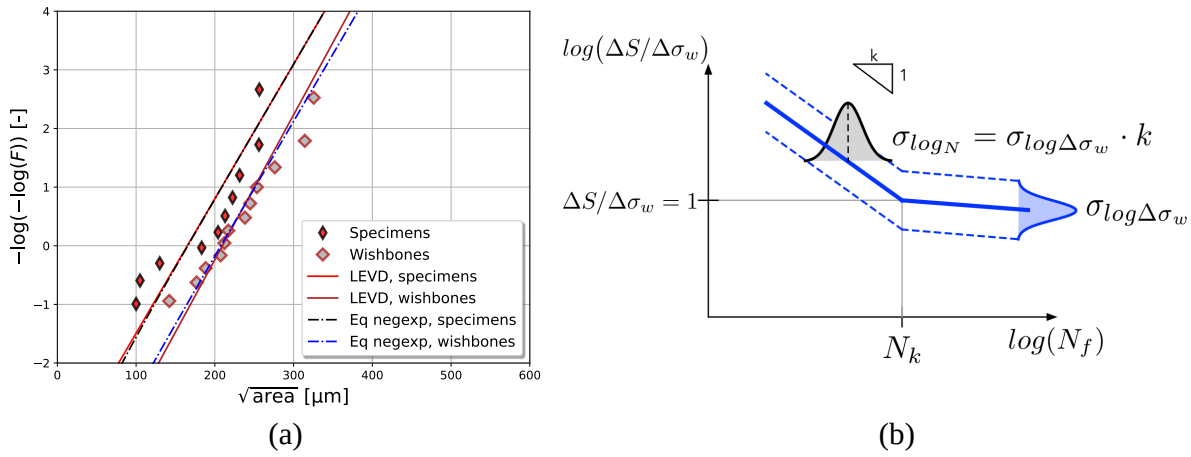

Figure 9: The two basic statistical variables in ProFACE: a) distribution of surface defects modelled as LEVD distribution and b) the relationship between scatter of $\sigma_{\log N}$ and that of $\Delta\sigma_{\mathrm{w}}$.

3.2.2. Inherent fatigue strength variability

Adopting a probabilistic model allows considering the inherent variability of the material properties (apart from the dependence on defects), which is essential to cover the *uncertainty* of the fatigue strength model. If we refer to the S-N model described above, it is clear that a variability of the fatigue life $\sigma_{\log N}$ is directly related to the dispersion of the fatigue strength $\sigma_{\log \Delta\sigma_{\mathrm{w}}}$, as schematically shown in Figure 9.b. Moreover, considering that the dispersion of the log-normal distribution corresponds to the coefficient of variation, the dispersion of the fatigue strength can be expressed by adopting the algebra of random variables as:

$$\left(\sigma_{\log N}/k\right)^2 = \left(\sigma_{\log \Delta\sigma_{\mathrm{w0}}}\right)^2 + \left(\frac{\partial\sigma_{\mathrm{w}}}{\partial a}\right)^2 \cdot \mathrm{CV}_a^2 \tag{7}$$

By adopting this formulation to the data of machined specimens, a scatter of $\sigma_{\log \Delta\sigma_{\mathrm{w0}}} = 0.03$ was calculated. This value is consistent with the variability of ΔK_{th} reported in ASTM-E647, and with the experimental

fatigue scatter measured on specimens.

3.3. Failure probability of a component

3.3.1. Weakest-link discretization

The weakest-link model implemented in ProFACE was originally elaborated for volumetric defects only, with a special development for calculating the *surface volume* where the randomly occurring defects have to be treated as surface cracks ($Y = 0.65$), [46].

Based upon the analogy between the typical rough surface of AM parts with equivalent elongated defects, the new ProFACE version schematises a component as in Figure 10.a. The external surface affected by the roughness is colored in red, the internal volume whose defects featured by a shape factor of $Y = 0.65$ is represented in green, while the volume on which the volumetric defects with a shape factor of $Y = 0.5$ belong is colored in blue. Each of the three parts can be then discretised in sub-areas and sub-volumes as shown in Figure 10.b, with their own reliability that is function of the area or the volume. The reliability of the component (under a given load and number of cycles) can be thus calculated as:

$$\mathcal{R}_{\text{comp,tot}} = \prod_{i=1}^{N_{E,\text{surf}}} \mathcal{R}_{i,A} \cdot \prod_{i=1}^{N_{E,V_{\text{surf}}}} \mathcal{R}_{i,V_{\text{surf}}} \cdot \prod_{i=1}^{N_{E,V_{\text{int}}}} \mathcal{R}_{i,V_{\text{int}}} \tag{8}$$

where N_E is the generic number of elements used to discretise the component, distinguished in superficial ($N_{E,\text{surf}}$), those belonging to the region dominated by the superficial random defects ($N_{E,V_{\text{surf}}}$) and those belonging to the volumetric internal defects ($N_{E,V_{\text{int}}}$). Each of these elements is featured by its own reliability, namely superficial reliability of the i-th superficial element $\mathcal{R}_{i,A}$, the reliability of the i-th volume governed by the random defects $\mathcal{R}_{i,V_{\text{surf}}}$ and finally the reliability of the i-th volume governed by the volumetric internal defects $\mathcal{R}_{i,V_{\text{int}}}$.

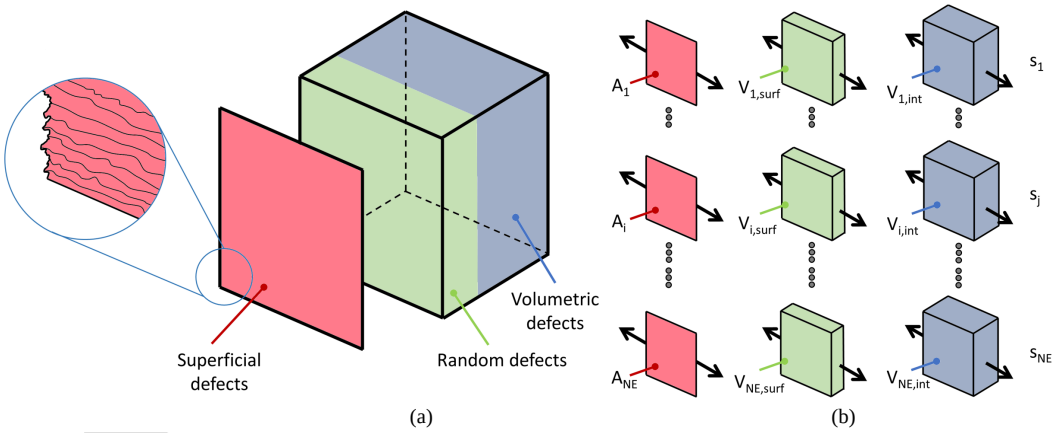

Figure 10: Schematic of the analysis performed by ProFACE: a) distinction between volumetric and superficial analysis and b) weakest link applied to both volumes and surfaces.

This method is at the bases of ProFACE [46], in which the stresses computed at the FE's integration points with their associated volume are considered for the application of Equation (4) to random volumetric defects.

A similar approach is then adopted for surface features. First the stress tensor is reconstructed on the surface nodes and a "nodal area" is computed by considering the dual graph to the surface FE triangularization. The weakest-link approach can then be applied considering the stress tensor at each surface node, with its nodal area.

3.3.2. Calculation of failure probability

The application of Equation (8) allows to calculate the reliability of the component considering the random occurrence of volumetric defects and surface features described by their *extreme value* distributions. The effect of other random variables (in this application the variability of the fatigue strength) can then be accounted with a numerical integration of the type:

$$\mathcal{R}_{\text{comp}} = \int_0^\infty \mathcal{R}_{\text{comp}}(\Delta\sigma_{\text{w0}}) \cdot f(\Delta\sigma_{\text{w0}}) \cdot d\Delta\sigma_{\text{w0}} \tag{9}$$

where $\mathcal{R}_{\text{comp}}(\Delta\sigma_{\text{w0}})$ is the reliability calculated for a given $\Delta\sigma_{\text{w0}}$ value and $f(\Delta\sigma_{\text{w0}})$ is the probability density function of the variable $\Delta\sigma_{\text{w0}}$. Other variables that can be considered with a similar computational scheme by ProFACE are: i) a random variable for the applied load (to represent the uncertainty of the model assumptions); ii) variability of the residual stresses (see Section 5.1).

The software calculates $P_{\text{f}} = 1 - \mathcal{R}_{\text{comp}}$ over a grid of F-N values chosen by the user. To provide an idea of the computational time, it takes about 917 s on a typical engineering workstation for calculating P_{f} over a grid of 1000 points for the FE model of 1/4 of the wishbone. The P_{f} surface is then suitably interpolated for plotting the F-N diagrams of the component with percentiles 2.5 %, 50 %, 97.5 % of the component life.

4. Application of ProFACE

ProFACE was used to estimate the fatigue life of standard uniaxial fatigue specimens and wishbones, in both machined and as-built state. These two different external surface states are featured by a different population of defects as well as different residual stress fields. The analyses were performed considering the defect distributions obtained from the dimension of the defects at the fracture origin of the specimens and the residual stress fields evaluated from the experimental measurements (see Tables 2 and 3).

4.1. Cylindrical samples

Uniaxial fatigue specimens, whose geometry is depicted in Figure 2.a, were numerically simulated with Abaqus Standard/2018. The material behaviour is assumed linear-elastic, since the specimens are tested in the HCF regime; the adopted Young's modulus is reported in Table 1, while the Poisson's ratio was considered equal to $\nu = 0.33$ as reported in technical engineering books for a general aluminium alloy at room temperature [64]. Exploiting the problem symmetries, only one eighth of the full geometry was analyzed by imposing the appropriate boundary conditions. A static force of 250 N (i.e., 1 kN for the full geometry) was applied on a reference point coupled with the gripping cylindrical surface at the top. The geometry was discretised with quadratic tetrahedral FEs, with a global mesh size of about 1 mm and a refined mesh size of about 0.2 mm in the gauge section; the mesh comprises 63 503 nodes and 41 919 elements in total. Under the hypothesis of linear-elastic behaviour, the calculations performed for different applied loads or surface conditions can be based on this unique FE analysis by multiplying the reference stress field by any user-defined loading factor (LF).

A compressive residual stress field was measured on the machined specimens having a nominal mean value of -76 MPa on the external surface oriented along the main specimen's axis, Table 2. It should be noted that a typical outcome of residual stress measurement is a 2D plain stress tensor associated to the surface under study. To be compliant with the experimental measurements, the residual stress tensor was remapped for each surface node in the Cartesian reference system of the simulated geometry to guarantee that the principal residual stress direction is tangent to the component's external surface. Being the external surface of the specimens machined, only the volumetric defects were considered; referring to the scheme of Figure 10.b, the weakest-link was then applied to the green and blue volumes. As a simplifying hypothesis, only the green volume of the scheme of Figure 10.b was considered affected by the compressive residual stress field, while the internal (blue) volume was considered to be unloaded and subjected only to the external loading cycle.

As-built specimens are affected by tensile residual stresses, with a nominal value of 60 MPa measured at the surface, Table 2. As experimental evidences showed that all failures originated from roughness-related surface features, the simulations with ProFACE were performed by applying the weakest-link on the external red surface of Figure 10.b, considering both the tensile residual stresses and the distribution of surface defects. In this case, the material volume controlled by the internal defects near the external surface (i.e., green part of Figure 10.b) was considered with the same residual stress. With this calculation scheme, a competition

between superficial features and volumetric defects near the surface is possible, even though surface defects are significantly larger than the volumetric ones. The residual stress tensor was re-mapped on the surface nodes also for as-built specimens.

The 95 % bilateral scatter bands estimated by ProFACE are compared with the experimental results in Figure 11. The estimations obtained for the machined specimens (Figure 11.a) considering the effect of residual stresses fit reasonably well with the experimental results, while neglecting the residual stresses provided conservative predictions compared to the experimental data-points. As for the as-built specimens (Figure 11.b), the fatigue limit is well estimated considering the residual stresses, while the estimations are conservative by increasing the stress range, with the experimental data-points closer to the results obtained neglecting residual stresses. This might be explained with the residual stress relaxation during the fatigue loading; at high stress ranges the sum of the maximum stress reached in the fatigue cycle with that residual can easily overcome the yield limit of the material, resulting in an elastic shake-down that can completely release the residual stress field [42, 66].

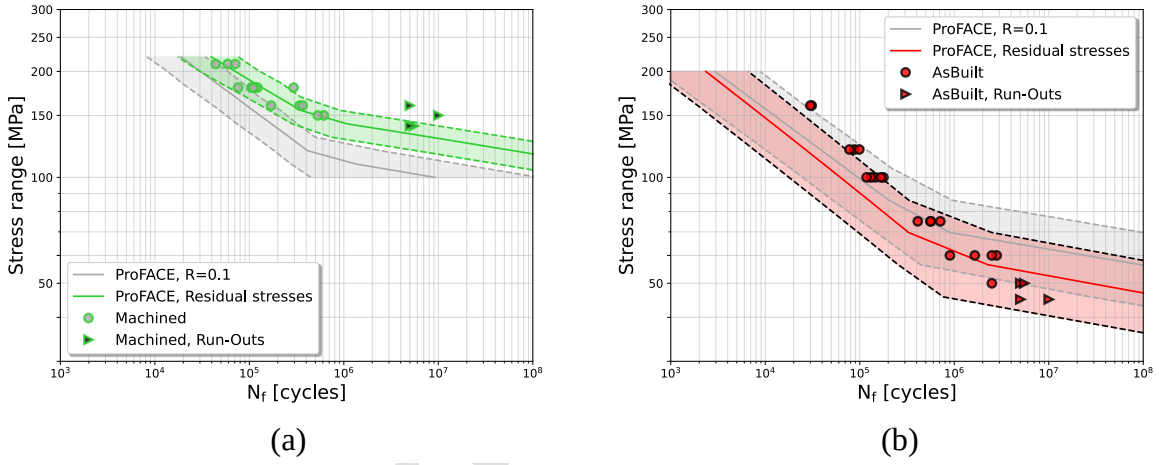

Figure 11: Failure probability estimated by ProFACE for the cylindrical specimens: a) machined fatigue specimens and b) as-built fatigue specimens.

4.2. Benchmark components

The capabilities of ProFACE were finally tested to evaluate the fatigue performances of the wishbone components. A reference FE simulation was first performed with Abaqus Standard/2018 considering the geometry of the printed parts shown in Figure 2.b. The simulated model was obtained by exploiting the symmetries of the part, hence considering only one-fourth of it. The top head of the wishbones featured a thread, which guarantees a mechanical connection with the testing machine. The bottom part was connected to the testing machine by means of a pin. To simulate these constraints, the internal cylindrical surface of the head was tied to a reference point, onto which a maximum force of 1 kN was applied (i.e., 4 kN for the entire model); the cylindrical part of the wishbone's leg was tied with a second reference point, positioned

at the intersection of the pin hole axis and the X-symmetry plane. All the degrees of freedom of the nodes of the internal cylindrical surface of the leg were constrained to the reference point except the displacement along the X-direction, being the connection pin free to slide inside the holes. This reference point was free to rotate around the X-axis, while all the others degrees of freedom were fixed. A schematic of the simulated model with the boundary conditions and the applied reference force is shown in Figure 12.a and Figure 12.b.

Differently from the simulations performed on the cylindrical specimens, the hypothesis of having a nominal residual stress field constant along all the external surfaces of the machined wishbones is not valid. Considering the experimental measurements performed by means of XRD in [54], and reported in Table 3, two main surfaces were identified on the components with different values of residual stresses, namely *side* and *front* as shown in the schematic of Figure 12.c.

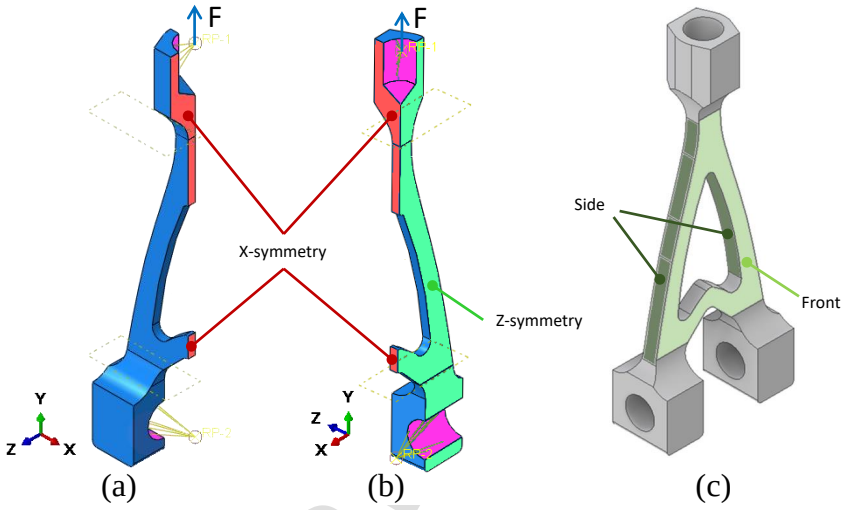

Figure 12: Scheme of the numerical simulations of the wishbones: a) frontal view of the load and boundary conditions; b) back view of the load and boundary conditions and c) zones of the application of different residual stress field.

Machined wishbones were simulated considering a compressive residual stress field with a nominal value of -100 MPa on the front surface and 60 MPa in tension on the side surface. Regarding to the as-built benchmark components, XRD measurements highlighted no particular difference between the side and front superficial values, hence a nominal tensile residual stress of 60 MPa was adopted. For the application of the weakest-link, the same approach used for the fatigue specimens was adopted for the benchmark components.

Finally, the ProFACE probabilistic estimates of both machined and as-built components were performed adopting the defect distributions obtained from the experimental campaign on the specimens. The numerical estimations obtained considering a 95 % bilateral scatter bands are compared with the experimental results in Figure 13.a and Figure 13.b for machined and as-built components, respectively.

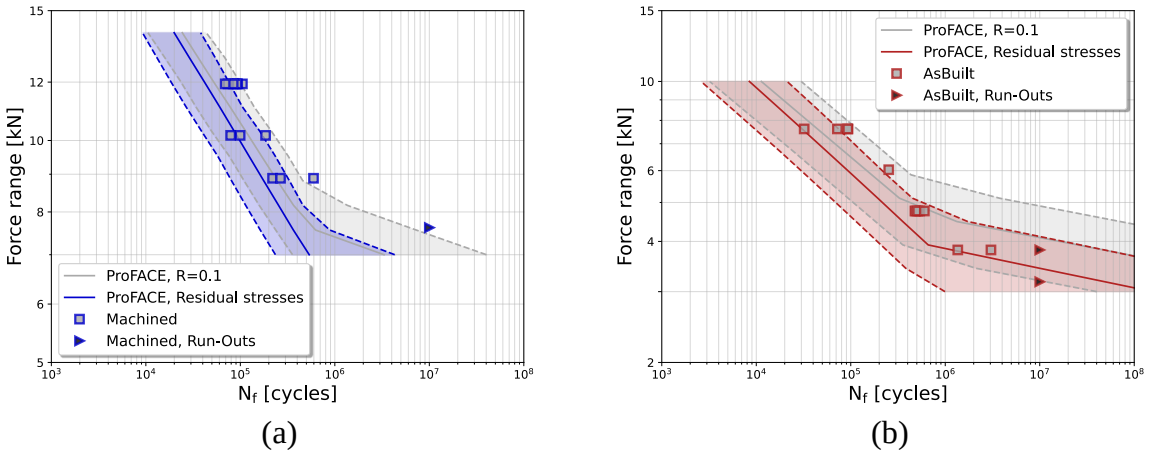

Figure 13: ProFACE analysis of wishbone specimens: a) machined wishbones and b) as-built wishbones.

The estimations of the machined wishbones considering the effect of residual stresses in Figure 13.a were found to overlap well with the experimental data; the estimations obtained neglecting the residual stress field were also satisfactory for the high force range levels. The numerical results obtained for the as-built wishbones in Figure 13.b considering the tensile residual stress field were found to fit well the experimental data-points in the fatigue limit zone, resulting, instead, in conservative estimations for the high levels of force ranges. These results reflect, in general, those found for the uniaxial fatigue specimens. Also for a local tensile residual stress field, stress relaxation is likely to occur at the highest stress levels.

4.3. Software outputs

In the preliminary fatigue design of a load-bearing component, it can be useful to visually identify the most critical locations for different scenarios. To fulfill this need, several visualization outputs are available in ProFACE for the designer, which are:

- normalized failure probability;
- critical defect;
- defect that ensures a user defined failure probability.

The normalized failure probability $P_{\mathrm{f,norm}}$ provides a qualitative evaluation of the failure probability at any point of the component. This quantity is calculated considering a reference volume $V_{\mathrm{ref}} = 1$ mm, which allows performing a direct comparison of different regions of the component regardless the mesh size. $P_{\mathrm{f,norm}}$ is computed considering the average material parameters, hence no variability is introduced in the calculation.

The estimation of the prospective critical defect size in a certain location of the component is an important information, as it affects both part strength and the necessary accuracy of NDE. This quantity depends on material properties and applied stress only. The *critical defect* is computed inside ProFACE and showed as a contour map; this is defined as the critical defect computed with Equation (2) with a safety margin on the target fatigue life that, in this analysis, was taken $\eta = 4$ [2, 3, 74]. The contour map of the defect size can be also evaluated in ProFACE referring to a predefined failure probability $P_{\mathrm{f,target}}$, which might be a program or certification requirement. This quantity is calculated by using the fatigue strength model (see Section 3) that corresponds to the target failure probability (referring to the variability of $\Delta\sigma_{\mathrm{w0}}$). Future implementations are being developed with more refined approaches addressing the *sizing error* of a prospective NDE.

The results obtained for the wishbones are shown in Figure 14, while the normalized failure probabilities computed for the three failure locations are compared with those experimental in Table 7. The normalized failure probabilities in Table 7 were computed for the machined component considering a force range of $\Delta F = 11.93$ kN and a fatigue life of $N_f = 87\,000$ cycles, that corresponds to the mean experimental fatigue life for that applied force range. The estimations obtained resulted to be aligned to those obtained experimentally, considering the number of failures due to each critical location over the total number of wishbones tested.

The critical defect map, shown in Figure 14.a with a schematic of the calculation flow respect to the target life, was calculated for the as-built component considering a force range of $\Delta F = 4.76$ kN and a target fatigue life of $N_{f,\mathrm{target}} = 25\,000$ cycles. The minimum critical defect size results approximately $\sqrt{\mathrm{area}}_{\mathrm{crit}} = 300$ µm, which corresponds to almost the 90 % percentile of the defect distribution for as-built components [54]. The failure probability at $N_{f,\mathrm{target}} = 25\,000$ cycles results to be $P_{\mathrm{f}} = 5.5 \times 10^{-5}$, while the failure probability at $N_f = 100\,000$ cycles (4 times the target life) is approximately 2.4 %. The latter value is surely larger that what could be calculated by experiment, but it reflects the conservatism of the life predictions.

It is interesting to consider the map from the point of view of NDE or prospective surface treatment selection. In details, most component regions have a critical defect size larger than 1 mm, a size that could be easily detected by NDE. Moreover, the critical defect of 300 µm only occurs at locations P2 and P3. The application of a local surface treatment in these regions (i.e., able to remove the surface features or to induce a compressive residual stress) would result in a large improvement of the whole component failure probability.

The critical defect size map for a predefined failure probability of $P_{\mathrm{f,target}} = 1 \times 10^{-4}$ was computed for the as-built component as showed in Figure 14.b, with a schematic representation of the target failure probability with the target life, considering again force range of $\Delta F = 4.76$ kN and a target fatigue life of $N_f = 25\,000$ cycles. As it can be seen, the minimum defect becomes $\min\left[\sqrt{\mathrm{area}}_{P_{\mathrm{f}}=1\times10^{-4}}\right] = 441$ µm, which is larger than that evaluated for $P_{\mathrm{f}} = 5.5 \times 10^{-5}$.

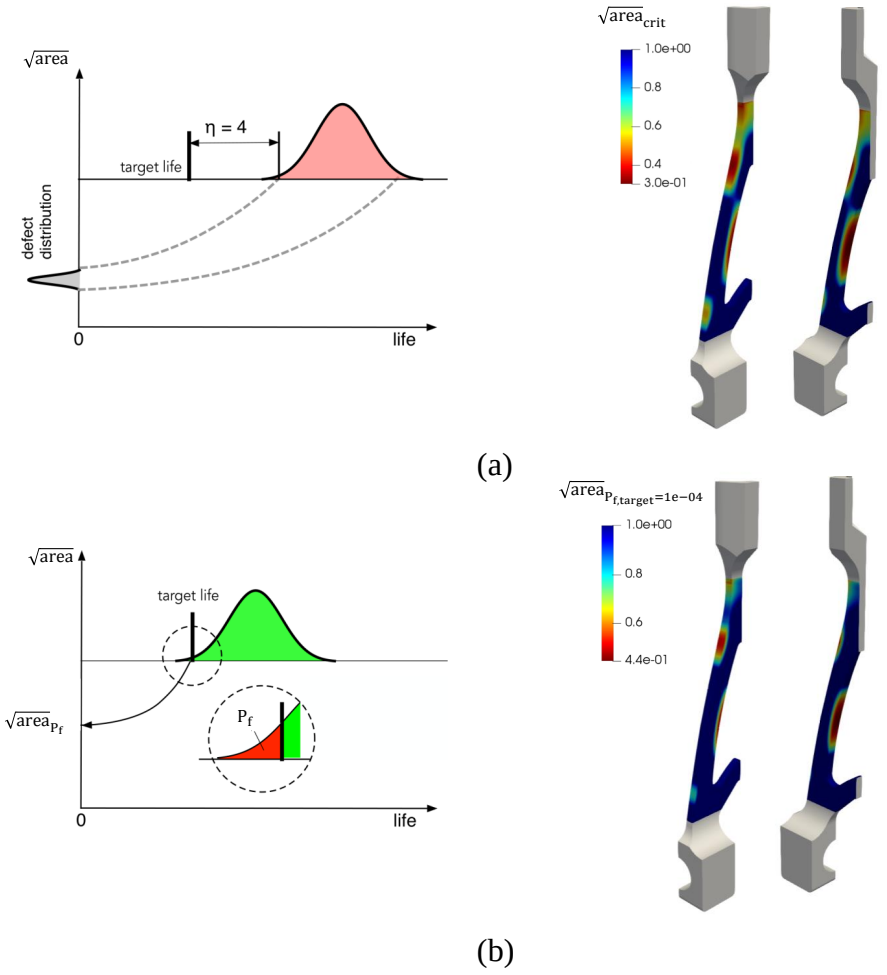

Figure 14: ProFACE visual outputs of the as-built benchmark component: a) schematic of the critical defect size considering a safety margin on the target life of $\eta = 4$ and the critical defect size map computed for the wishbone at $\Delta F = 4.76$ kN and $N_{f,\mathrm{target}} = 25\,000$ cycles and b) schematic of the critical defect size considering a predefined target failure probability and the critical defect size map at a target failure probability of $P_{\mathrm{f,target}} = 1 \times 10^{-4}$ at $\Delta F = 4.76$ kN and $N_f = 25\,000$ cycles.

Table 7: Comparison between the experimental and numerical estimation of the normalised failure probabilities of failure locations of the wishbones schematically reported in Figure 4.b

	P1	P2	P3
Experimental	0.04	0.48	0.48
Numerical	0.09	0.25	0.65

5. Sensitivity analysis

Fatigue tests are typically affected by a certain level of uncertainty. Besides the presence of manufacturing defects, variability of the material resistance $\Delta\sigma_{w0}$, and possible uncertainty on the applied stress, which were all included in the first version of ProFACE [46], other variables might affect the final life prediction. In the previous section it was shown how the effect of residual stresses can influence the fatigue resistance of specimens and components. Moreover, it is well known that residual stress measurements suffer from poor repeatability and non-negligible uncertainty. Similarly, also the defect population caused by the AM process might vary, especially from the point of view of defect occurrence rate, for example related to the position on the platform [75, 76, 77].

Therefore, the question arises on how the uncertainty of these two inputs might effect the component life prediction, which is the topic of this section.

5.1. Variability of residual stresses

To analyse the effect of the uncertainty of residual stress measurements in machined wishbones, analyses similar to the ones in Section 4.2 were repeated by applying the maximum or minimum measured value at the different locations [54]. The surfaces named *front* in Figure 12.c showed a different residual stress field than the *side* ones. Hence, two analyses were performed varying once at a time the applied residual stress field. The residual stress values adopted are reported in Table 8 and schematically showed in Figure 15.a. The NASGRO curve for the long crack threshold fitted for the AlSi10Mg considered in this work [54], showed a flat trend in the positive stress ratio region. Due to this, the fatigue estimations of ProFACE are mainly insensible to a variation of the residual stress in tension, and hence this analysis was not reported for the as-built wishbones.

Table 8: Summary of the residual stress values adopted for the sensitivity analyses on machined wishbones.

Analyses	σ_{RS}^{front} [MPa]	σ_{RS}^{side} [MPa]
1	-100.0	0.0
2	-100.0	130.0
3	-50.0	65.0
4	-150.0	65.0

The obtained numerical estimations are compared with the experimental results in Figure 15. It can be noted that the variation of the residual stress field on the front surfaces has basically no effect in the obtained F-N curves (Figure 15.b), while the variation of residual stress field in the side surfaces (Figure 15.c) impacts the numerical estimations, especially in the endurance limit region. The most stressed zones of the wishbone are located on the side surfaces, this can explain the higher variation of fatigue estimations by varying the residual stress values there.

Considering that the variability of the residual stresses on the front surfaces has negligible effect on the numerical fatigue estimations obtained, only the variability of side surfaces was considered, while the average residual stress was maintained on the front surfaces. The two extremes of the residual stress values in Figure 15.c where numerically discretised supposing an uniform distribution of residual stress in five equispaced values. The results obtained were averaged to calculate a failure probability representative of the statistical variability of the residual stresses. Figure 15.d compares the bilateral 95 % scatter bands against the experimental results. The estimations were found to fit fairly well the experimental data-points, which confirms the benefit of studying fatigue performances of an AMed components from a probabilistic point of view.

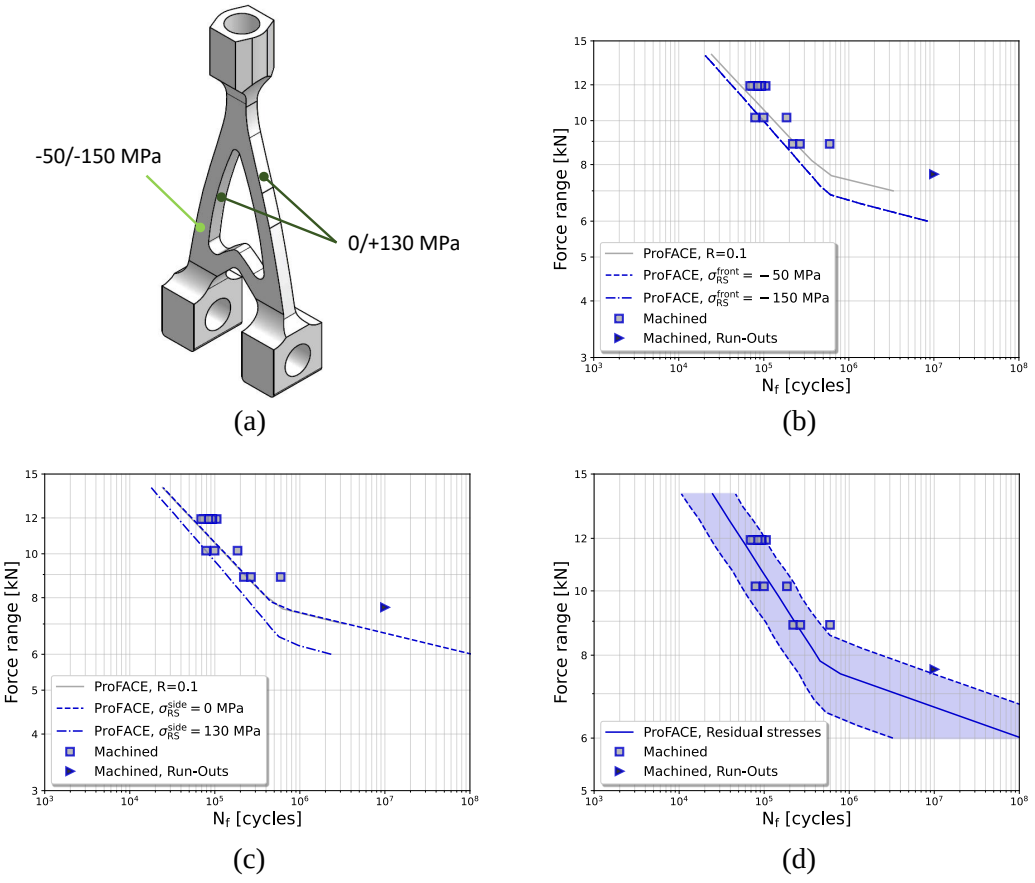

Figure 15: Numerical estimations of the machined wishbones considering the residual stress variability: a) schematic of the variability of the measured residual stresses onto the side and front surfaces; b) sensitivity analysis considering the variability of the residual stresses onto the front surface; c) sensitivity analysis considering the variability of the residual stresses onto the side surface and d) ProFACE results obtained from a series of analyses considering a uniform distribution of the residual stresses.

5.2. Defect distribution

By applying Equation (5) to the volumetric defects detected on machined specimens and wishbones, it can be seen that the LEVD estimated from specimens (applying Equation (5)) is the lower bound of defect

distribution estimated from components. It is known that defect distribution depends on the local thermal history [78] and on the gas shielding flow [79]. Accordingly, it looks reasonable that the printed wishbones could have defects more scattered than those of specimens' gauge volume.

To account for this ineluctable variability of defect population, sensitivity analyses were carried out considering the upper bound of the distribution of defects in Table 6 (red line in Figure 16.a) considering for wishbones a LEVD distribution with parameters:

$$\tilde{\lambda} = 75 \text{ µm} \quad \tilde{\delta} = 18 \text{ µm} \tag{10}$$

The analyses with two scenarios (defect distribution inferred from specimens' data and upper bound of wishbone data) showed that the effect in terms of average fatigue life is not significant (Figure 16.b), but it can be appreciated that the upper bound distribution provides a more conservative scenario for a prospective design due to the larger defect size scatter. From this point of view, the key parameter of the LEVD is δ, as it controls the scatter.

It is of some importance to remark that the upper bound value for the ProFACE simulations could have been estimated as the value corresponding to the upper 99 % confidence from the defect data on specimens, adopting sampling distributions of LEVD estimators [80, 81]. This means that a proper statistical analysis of the defect data from specimens could have provided a realistic *upper bound* scenario.

6. Limitations and future developments

The hypotheses on which the software is based (namely the description of fatigue life through the normalized S-N diagram in Figure 7) limit its present capabilities to engineering applications in HCF. ProFACE aims at covering the present gap between simple weakest-link analyses and detailed probabilistic crack growth tools with a quick post-processor based on defect-tolerance concepts. Future developments, aimed at keeping this main peculiarity, will extend its capabilities in the following directions:

- extension to multiaxial fatigue to include the conclusions reached in recent fatigue campaigns on AlSi10Mg and Ti6Al4V [82, 83];
- maps $\Delta\sigma_{w0} - N_f$ obtained by integration of the NASGRO crack propagation equation with terms for including elasto-plastic crack driving force [13];
- criteria for defect/flaw assessment that consider the combination of different load cases and load spectra.

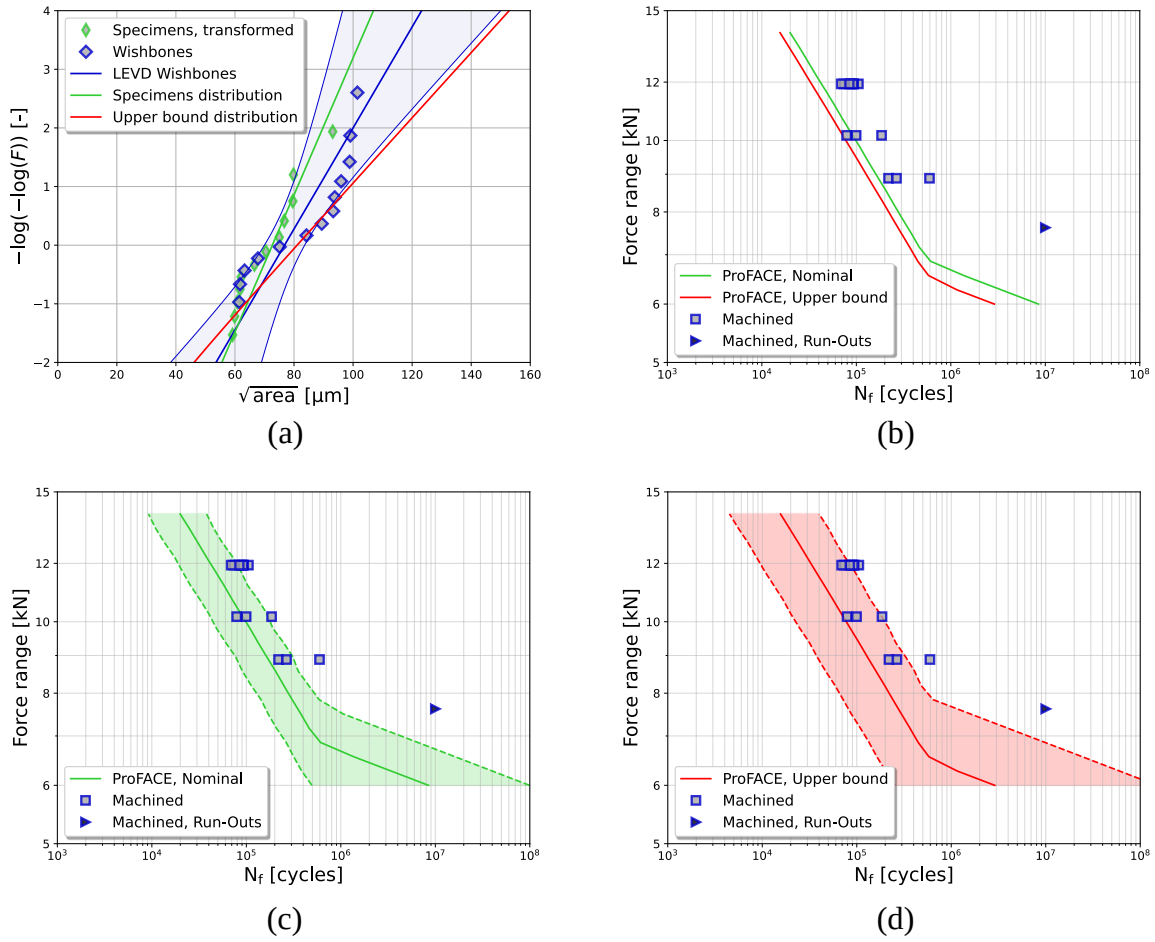

Figure 16: Sensitivity to defect distribution parameters: a) fitting of the distributions with different parameters (specimen data transformed to the volume of wishbones through Eq. (4)); b) effect of the parameters' distribution for the 50 % percentile life estimate; c) 95 % bilateral scatter bands for the average defect distribution and d) 95 % bilateral scatter bands for the upper bound defect distribution.

7. Conclusions

AMed metal parts have opened new design possibilities to solve engineering problems based on geometry optimization and high structural strength over weight ratio. However, there is the need (reflected in guidances developed by NASA and ESA) of design rules able to account for the presence of volumetric and surface anomalies, and the presence of residual stresses. If fracture-based life estimations work well for AMed materials at the specimen level, the application of similar approaches to components is not so straightforward and requires probabilistic tools for considering many key parameters such as loads, material properties, anomalies, residual stresses, and their variability.

To overcome these limitations, the probabilistic software ProFACE was developed to estimate the fatigue strength and failure probability of load-bearing components manufactured by AM. The aim of this work was to extend the capabilities of the software and validate it on a wide benchmark test campaign on specimens and components. By comparing the numerical estimations with the experimental results, the following conclusions can be drawn.

1. The fatigue strength of both uniaxial fatigue specimens and wishbones is highly affected by the statistical variability of volumetric defects (for machined parts) and superficial features (for as-built parts). This effect is accounted by a weakest-link approach, which incorporates extremes value distributions for both volumetric and superficial defects.
2. Beside the influence of anomalies, residual stresses play the major role in determining the fatigue strength of AMed parts made of *as-built* Al-alloy components. This effect is managed by adopting a fatigue strength model that depends on the defect size and the effective stress ratio calculated from the local residual stress field and the stress tensor due to component loads.
3. The typical sources of variability and experimental uncertainties were then tackled via ProFACE simulations. The obtained results were found to describe fairly good the experimental data-points obtained, highlighting the flexibility of probabilistic approaches during the design phase.
4. The ProFACE post-processor was shown to provide fast and fairly accurate estimates of the failure probability of AM components, as well as various visualization options that can be a valuable asset for both the design and verification phases.

8. Acknowledgements

The authors acknowledge the support of the European Space Agency trough contract n. 4000120221-17-NL-LvH, in which MTC contracted Politecnico di Milano for "ProFACE Benchmark" according to ESA-TRP-TECMSP-SOW-009494, and contract n. 4000133245/20/NL/AR/idb, in which MTC contracted Politecnico di Milano for "ProFACE surface features extension" according to ESA-TRP-TECMSP-SOW-009494.

The authors thank the European Space Agency, especially Dr. Tommaso Ghidini, for permission to publish the results of the activities developed within those contracts.

Author contributions

Contributions to this paper are as follows: (i) F. Sausto developed the new software features presented in the paper, he took care of the numerical analyses and the preparation of the manuscript; (ii) S. Romano designed the benchmark component, contributed to the initial software development, he also contributed to the preparation and final revision of the manuscript; (iii) L. Patriarca performed and supervised the whole experimental campaign reported in this work, he contributed to the preparation and final review of the manuscript; (iv) S. Miccoli contributed to the code optimization and to the development of the numerical strategies adopted in the software, he contributed to the final review of the manuscript; (v) S. Beretta directed this research activity and the software development, took care of extreme value models adopted in the software, he contributed to the preparation and revision of the manuscript.

Disclaimer

There are no commercial interests associated with this publication that could have influenced its outcomes. The software in the version here described will be installed at the European Space Agency (ESTEC, Structures Section) as part of the current contracts mentioned in the Acknowledgements section.

References

[1] M. Gorelik, Additive manufacturing in the context of structural integrity, International Journal of Fatigue 94 (2017) 168–177. doi:10.1016/j.ijfatigue.2016.07.005.

[2] ECSS-Q-ST-70-80C, Space Product Assurance - Processing and Quality Assurance Requirements for Metallic Powder Bed Fusion Technologies for Space Applications (2021).

[3] McElroy, A Summary of NASA-HDBK-5026: Guidance on strength, fatigue, and fracture control requirements for additive manufactured spaceflight hardware, Presentation at ICAM 2021, available at: https://ntrs.nasa.gov/citations/20210020710 (2021).
URL https://ntrs.nasa.gov/citations/20210020710

[4] A. Martínez-García, M. Monzón, R. Paz, Chapter 12 - standards for additive manufacturing technologies: structure and impact, in: J. Pou, A. Riveiro, J. P. Davim (Eds.), Additive Manufacturing, Handbooks in Advanced Manufacturing, Elsevier, 2021, pp. 395–408. doi:https://doi.org/10.1016/B978-0-12-818411-0.00013-6.

[5] J. Gumpinger, M. Seifi, N. Shamsaei, C. Seidel, R. W. Russell, 20 - recent progress on global standardization, in: I. Yadroitsev, I. Yadroitsava, A. du Plessis, E. MacDonald (Eds.), Fundamentals of Laser Powder Bed Fusion of Metals, Additive Manufacturing Materials and Technologies, Elsevier, 2021, pp. 563–582. doi:https://doi.org/10.1016/B978-0-12-824090-8.00021-4.

[6] A. Mostafaei, C. Zhao, Y. He, S. R. Ghiaasiaan, B. Shi, S. Shao, N. Shamsaei, Z. Wu, N. Kouraytem, T. Sun, et al., Defects and anomalies in powder bed fusion metal additive manufacturing, Current Opinion in Solid State and Materials Science 26 (2) (2022) 100974.

[7] M. Grasso, B. M. Colosimo, Process defects and in situ monitoring methods in metal powder bed fusion: a review, Measurement Science and Technology 28 (4) (2017) 044005.

[8] A. Sola, A. Nouri, Microstructural porosity in additive manufacturing: The formation and detection of pores in metal parts fabricated by powder bed fusion, Journal of Advanced Manufacturing and Processing 1 (3) (2019) e10021.

[9] X. Peng, L. Kong, H. An, G. Dong, A review of in situ defect detection and monitoring technologies in selective laser melting, 3D Printing and Additive Manufacturing (2022).

[10] S. Romano, A. D. Brandão, J. Gumpinger, M. Gschweitl, S. Beretta, Qualification of AM parts: Extreme value statistics applied to tomographic measurements, Materials & Design 131 (May) (2017) 32–48. doi:10.1016/j.matdes.2017.05.091.

[11] N. Sanaei, A. Fatemi, N. Phan, Defect characteristics and analysis of their variability in metal L-PBF additive manufacturing, Materials and Design 182 (2019) 108091. doi:10.1016/j.matdes.2019.108091.

[12] U. Zerbst, G. Bruno, J. Y. Buffière, T. Wegener, T. Niendorf, T. Wu, X. Zhang, N. Kashaev, G. Meneghetti, N. Hrabe, M. Madia, T. Werner, K. Hilgenberg, M. Koukolíková, R. Procházka, J. Džugan, B. Möller, S. Beretta, A. Evans, R. Wagener, K. Schnabel, Damage tolerant design of additively manufactured metallic components subjected to cyclic loading: State of the art and challenges, Progress in Materials Science 121 (2021) 100786. doi:10.1016/j.pmatsci.2021.100786.

[13] S. Romano, A. Brückner-Foit, A. Brandão, J. Gumpinger, T. Ghidini, S. Beretta, Fatigue properties of alsi10mg obtained by additive manufacturing: Defect-based modelling and prediction of fatigue strength, Engineering Fracture Mechanics 187 (2018) 165–189. doi:10.1016/j.engfracmech.2017.11.002.

[14] S. Romano, L. Patriarca, S. Foletti, S. Beretta, LCF behaviour and a comprehensive life prediction model for AlSi10Mg obtained by SLM, International Journal of Fatigue 117 (July) (2018) 47–62. doi:10.1016/j.ijfatigue.2018.07.030.

[15] N. Sanaei, A. Fatemi, Defect-based fatigue life prediction of l-pbf additive manufactured metals, Engineering Fracture Mechanics 244 (2021) 107541.

[16] R. Molaei, A. Fatemi, N. Sanaei, J. Pegues, N. Shamsaei, S. Shao, P. Li, D. Warner, N. Phan, Fatigue of additive manufactured ti-6al-4v, part ii: The relationship between microstructure, material cyclic properties, and component performance, International Journal of Fatigue 132 (2020) 105363.

[17] S. Beretta, M. Gargourimotlagh, S. Foletti, A. Du Plessis, M. Riccio, Fatigue strength assessment of "as built" alsi10mg manufactured by slm with different build orientations, International Journal of Fatigue 139 (2020) 105737.

[18] M. H. Nasab, S. Romano, D. Gastaldi, S. Beretta, M. Vedani, Combined effect of surface anomalies and volumetric defects on fatigue assessment of AlSi7Mg fabricated via laser powder bed fusion, Additive Manufacturing (2019). doi:10.1016/j.addma.2019.100918.

[19] J. Gumpinger, A. D. Brandão, E. Beevers, T. Rohr, T. Ghidini, S. Beretta, S. Romano, Expression of Additive Manufacturing Surface Irregularities Through a flaw-Based Assessment, ASTM Selected Technical Papers 1620 (2019).

[20] J. W. Pegues, N. Shamsaei, M. D. Roach, R. S. Williamson, Fatigue life estimation of additive manufactured parts in the as-built surface condition, Material Design & Processing Communications 1 (3) (2019) e36, e36 MDPC-2018-025.R1. arXiv:https://onlinelibrary.wiley.com/doi/pdf/10.1002/mdp2.36, doi:https://doi.org/10.1002/mdp2.36.
URL https://onlinelibrary.wiley.com/doi/abs/10.1002/mdp2.36

[21] E. Wycisk, A. Solbach, S. Siddique, D. Herzog, F. Walther, C. Emmelmann, Effects of defects in laser additive manufactured Ti-6Al-4V on fatigue properties, Physics Procedia 56 (C) (2014) 371–378. doi:10.1016/j.phpro.2014.08.120.

[22] D. Greitemeier, F. Palm, F. Syassen, T. Melz, Fatigue performance of additive manufactured TiAl6V4 using electron and laser beam melting, Int. J. Fatigue (2016) 1–7doi:10.1016/j.ijfatigue.2016.05.001.

[23] A. Yadollahi, M. J. Mahtabi, A. Khalili, H. R. Doude, J. C. Newman, Fatigue life prediction of additively manufactured material: Effects of surface roughness, defect size, and shape, Fatigue and Fracture of Engineering Materials and Structures 41 (7) (2018) 1602–1614. doi:10.1111/ffe.12799.

[24] M. Nakatani, H. Masuo, Y. Tanaka, Y. Murakami, Effect of Surface Roughness on Fatigue Strength of Ti-6Al-4V Alloy Manufactured by Additive Manufacturing, Procedia Structural Integrity 19 (2019) 294–301. doi:10.1016/j.prostr.2019.12.032.

[25] J. Zhang, A. Fatemi, Surface roughness effect on multiaxial fatigue behavior of additive manufactured metals and its modeling, Theoretical and Applied Fracture Mechanics 103 (2019). doi:10.1016/j.tafmec.2019.102260.

[26] S. Romano, P. D. Nezhadfar, S. Beretta, M. Seifi, N. Shamsaei, High cycle fatigue behavior and life prediction for additively manufactured 17-4 PH stainless steel: Effect of sub-surface porosity and surface roughness, Theoretical and Applied Fracture Mechanics 106 (April) (2020) 102477. doi:10.1016/j.tafmec.2020.102477.

[27] Federal Aviation Administration, AC 33.70-1 - Guidance Material for Aircraft Engine Life-Limited Parts Requirements - chg 1, Tech. rep., U.S. Department of Transportation (2017).

[28] ECSS-E-ST-32-01C Rev. 1, Space engineering - Fracture control (2009).

[29] NASA, Fracture Control Requirements For Spaceflight Hardware, NASA fracture control (2016) 119. URL https://standards.nasa.gov/standard/nasa/nasa-std-5019

[30] Federal Aviation Administration, AC 33.14-1 - Damage Tolerance for High Energy Turbine Engine Rotors (2001).

[31] Federal Aviation Administration, AC 33.70-2 - Damage Tolerance of Hole Features in High-Energy Turbine (2009).

[32] A. du Plessis, I. Yadroitsava, I. Yadroitsev, Effects of defects on mechanical properties in metal additive manufacturing: A review focusing on X-ray tomography insights, Materials and Design 187 (2020). doi:10.1016/j.matdes.2019.108385.

[33] A. du Plessis, S. G. le Roux, Standardized X-ray tomography testing of additively manufactured parts: A round robin test, Additive Manufacturing 24 (2018) 125–136. doi:https://doi.org/10.1016/j.addma.2018.09.014.

[34] A. du Plessis, I. Yadroitsev, I. Yadroitsava, S. G. Le Roux, X-Ray Microcomputed Tomography in Additive Manufacturing: A Review of the Current Technology and Applications, 3D Printing and Additive Manufacturing 5 (3) (2018) 3d2018.0060. doi:10.1089/3dp.2018.0060.

[35] Z. Wu, S. Wu, J. Bao, W. Qian, S. Karabal, W. Sun, P. Withers, The effect of defect population on anisotropic fatigue resistance of selective laser melted alsi10mg alloy, International Journal of Fatigue (2021) 106317.

[36] S. Romano, A. Abel, J. Gumpinger, A. D. Brandão, S. Beretta, Quality control of AlSi10Mg produced by SLM: metallography versus CT scans for critical defect size assessment, Additive Manufacturing 28 (2019) 394–405. doi:10.1016/j.addma.2019.05.017.

[37] NASA, MSFC-STD-3716 - Standard for Additively Manufactured Spaceflight Hardware By Laser Powder Bed Fusion (2017).

[38] M. Kahlin, H. Ansell, D. Basu, A. Kerwin, L. Newton, B. Smith, J. J. Moverare, Improved fatigue strength of additively manufactured Ti6Al4V by surface post processing, International Journal of Fatigue 134 (2020) 105497. doi:10.1016/j.ijfatigue.2020.105497.

[39] E. Beevers, A. D. Brandão, J. Gumpinger, M. Gschweitl, C. Seyfert, P. Hofbauer, T. Rohr, T. Ghidini, Fatigue properties and material characteristics of additively manufactured AlSi10Mg – Effect of the contour parameter on the microstructure, density, residual stress, roughness and mechanical properties, International Journal of Fatigue 117 (April) (2018) 148–162. doi:10.1016/j.ijfatigue.2018.08.023.

[40] M. W. McElroy, S. Luna, R. Patin, Fracture Control for Additive Manufactured Spacecraft Structures, in: 70th International Astronautical Congress (IAC), Washington D.C., 2019, pp. IAC–19–C2.1.3.

[41] R. Russell, D. Wells, J. Waller, B. Poorganji, E. Ott, T. Nakagawa, H. Sandoval, N. Shamsaei, M. Seifi, 3 - qualification and certification of metal additive manufactured hardware for aerospace applications, in: F. Froes, R. Boyer (Eds.), Additive Manufacturing for the Aerospace Industry, Elsevier, 2019, pp. 33–66. doi:https://doi.org/10.1016/B978-0-12-814062-8.00003-0.

[42] F. Sausto, C. Tezzele, S. Beretta, Analysis of fatigue strength of l-pbf alsi10mg with different surface post-processes: Effect of residual stresses, Metals 12 (6) (2022) 898.

[43] A. Karolczuk, et al., Validation of the weakest link approach and the proposed weibull based probability distribution of failure for fatigue design of steel welded joints, Engineering Failure Analysis 67 (2016) 46–62.

[44] A. Wormsen, B. Sjödin, G. Härkegård, A. Fjeldstad, Non-local stress approach for fatigue assessment based on weakest-link theory and statistics of extremes, Fatigue & Fracture of Engineering Materials & Structures 30 (12) (2007) 1214–1227.

[45] P. Li, D. Warner, N. Phan, Predicting the fatigue performance of an additively manufactured ti-6al-4v component from witness coupon behavior, Additive manufacturing 35 (2020) 101230.

[46] S. Romano, S. Miccoli, S. Beretta, A new fe post-processor for probabilistic fatigue assessment in the presence of defects and its application to am parts, International Journal of Fatigue 125 (2019) 324–341.

[47] A. Fjeldstad, A. Wormsen, G. Härkegård, Simulation of fatigue crack growth in components with random defects, Engineering Fracture Mechanics 75 (5) (2008) 1184–1203.

[48] A. Wormsen, A. Fjeldstad, G. Härkegård, A post-processor for fatigue crack growth analysis based on a finite element stress field, Computer Methods in Applied Mechanics and Engineering 197 (6-8) (2008) 834–845. doi:10.1016/j.cma.2007.09.012.

[49] M. Enright, S. Hudak, R. McClung, Application of Probabilistic Fracture Mechanics to Prognosis of Aircraft Engine Components, AIAA Journal (2006) 311–316.

[50] G. Leverant, H. Millwater, R. McClung, M. Enright, A new tool for design and certification of aircraft turbine rotors, J. Engng Gas Turbines Power 126 (2004) 155–159.

[51] R. McClung, , M. Enright, H. Millwater, G. Leverant, S. Hudak, A software Framework for Probabilistic Fatigue Life Assessment of Gas Turbine Engine Rotor, J. ASTM Int. 1 (8) (2004).

[52] R. C. McClung, Y.-D. Lee, W. Liang, M. P. Enright, S. H. K. Fitch, Automated fatigue crack growth analysis of components, Procedia Eng. 2 (1) (2010) 629–637. doi:http://dx.doi.org/10.1016/j.proeng.2010.03.068.

[53] M. P. Enright, R. C. McClung, J. C. Sobotka, J. P. Moody, J. McFarland, Y.-D. Lee, I. Gray, J. Gray, Influences of non-destructive inspection simulation on fracture risk assessment of additively manufactured turbine engine components, in: Turbo Expo: Power for Land, Sea, and Air, Vol. 51135, American Society of Mechanical Engineers, 2018, p. V07AT32A013.

[54] S. Beretta, L. Patriarca, M. Gargourimotlagh, A. Hardaker, D. Brackett, M. Salimian, J. Gumpinger, T. Ghidini, A benchmark activity on the fatigue life assessment of AlSi10Mg components manufactured by L-PBF, Materials & Design (2022).

[55] ASTM E466-21, Standard Practice for Conducting Force Controlled Constant Amplitude Axial Fatigue Tests of Metallic Materials1 (2021). doi:10.1520/E0466-21.

[56] ASTM, E739-10 Standard Practice for Statistical Analysis of Linear or Linearized Stress-Life (S-N) and Strain-Life (ϵ-N) Fatigue Data, Tech. rep., American Sosciety for Testing and Materials, West Conshohocken, PA (2015). doi:https://doi.org/10.1520/E0739-10R15.

[57] W. J. Dixon, The up-and-down method for small samples, Journal of the American Statistical Association 60 (312) (1965) 967–978.

[58] S. Beretta, More than 25 years of extreme value statistics for defects: Fundamentals, historical developments, recent applications, International Journal of Fatigue 151 (2021) 106407.

[59] S. Beretta, Affidabilità delle costruzioni meccaniche: Strumenti e metodi per l'affidabilità di un progetto, Springer Science & Business Media, 2010.

[60] M. El Haddad, T. Topper, K. Smith, Prediction of non propagating cracks, Engineering fracture mechanics 11 (3) (1979) 573–584.

[61] Y. Murakami, T. Takagi, K. Wada, H. Matsunaga, Essential structure of sn curve: Prediction of fatigue life and fatigue limit of defective materials and nature of scatter, International Journal of Fatigue 146 (2021) 106138.

[62] C. M. Sonsino, Course of sn-curves especially in the high-cycle fatigue regime with regard to component design and safety, International Journal of Fatigue 29 (12) (2007) 2246–2258.

[63] C. Sonsino, R. Franz, Multiaxial fatigue assessment for automotive safety components of cast aluminium en ac-42000 t6 (g-alsi7mg0. 3 t6) under constant and variable amplitude loading, International Journal of Fatigue 100 (2017) 489–501.

[64] N. E. Dowling, Mechanical behavior of materials: engineering methods for deformation, Fracture and Fatigue, (1999).

[65] J. Schijve, Fatigue of structures and materials, Springer, 2009.

[66] F. Sausto, P. Carrion, N. Shamsaei, S. Beretta, Fatigue failure mechanisms for alsi10mg manufactured by l-pbf under axial and torsional loads: the role of defects and residual stresses, International Journal of Fatigue (2022).

[67] T. Persenot, A. Burr, G. Martin, J.-Y. Buffiere, R. Dendievel, E. Maire, Effect of build orientation on the fatigue properties of as-built electron beam melted ti-6al-4v alloy, International Journal of Fatigue 118 (2019) 65–76.

[68] L. Sheridan, A modified el-haddad model for versatile defect tolerant design, International Journal of Fatigue 145 (2021) 106062.

[69] L. Sheridan, J. E. Gockel, O. E. Scott-Emuakpor, Stress-defect-life interactions of fatigued additively manufactured alloy 718, International Journal of Fatigue 143 (2021) 106033.

[70] S. Romano, L. Patriarca, S. Foletti, S. Beretta, Lcf behaviour and a comprehensive life prediction model for alsi10mg obtained by slm, International Journal of fatigue 117 (2018) 47–62.

[71] A. Wormsen, G. Härkegård, A statistical investigation of fatigue behaviour according to weibull's weakest link theory, ECF15 (2004).

[72] S. Beretta, C. Anderson, Y. Murakami, Extreme Value Models for the Assessment of Steels Containing Multiple Types of Inclusion, Acta Materialia 5 (54) (2006) 2277–2289.

[73] S. Romano, P. Nezhadfar, N. Shamsaei, M. Seifi, S. Beretta, High cycle fatigue behavior and life prediction for additively manufactured 17-4 ph stainless steel: Effect of sub-surface porosity and surface roughness, Theoretical and Applied Fracture Mechanics 106 (2020) 102477.

[74] NASA, MSFC-SPEC-3717 - Specification for Control and Qualification of Laser Powder Bed Fusion Metallurgical Processes (2017).

[75] P. Li, D. Warner, A. Fatemi, N. Phan, Critical assessment of the fatigue performance of additively manufactured ti–6al–4v and perspective for future research, International Journal of Fatigue 85 (2016) 130–143.

[76] J. Günther, S. Leuders, P. Koppa, T. Tröster, S. Henkel, H. Biermann, T. Niendorf, On the effect of internal channels and surface roughness on the high-cycle fatigue performance of ti-6al-4v processed by slm, Materials & Design 143 (2018) 1–11.

[77] P. Li, D. Warner, J. Pegues, M. Roach, N. Shamsaei, N. Phan, Towards predicting differences in fatigue performance of laser powder bed fused ti-6al-4v coupons from the same build, International Journal of Fatigue 126 (2019) 284–296.

[78] A. Yadollahi, N. Shamsaei, Additive manufacturing of fatigue resistant materials: Challenges and opportunities, International Journal of Fatigue 98 (2017) 14–31.

[79] T. Moran, D. Warner, A. Soltani-Tehrani, N. Shamsaei, N. Phan, Spatial inhomogeneity of build defects across the build plate in laser powder bed fusion, Additive Manufacturing 47 (2021) 102333.

[80] S. Beretta, Y. Murakami, Statistical Analysis of Defects for Fatigue Strength Prediction and Quality Control of Materials, Fatigue Fract. Eng. Mater. Struct. 21 (9) (1998) 1049–1065. doi:doi:10.1046/j.1460-2695.1998.00104.x.

[81] R. Reiss, M. Thomas, Statistical Analysis of Extreme Values, Birkhauser Verlag, Basel, 1997.

[82] F. Sausto, P. Carrion, N. Shamsaei, S. Beretta, Fatigue failure mechanisms for alsi10mg manufactured by l-pbf under axial and torsional loads: The role of defects and residual stresses, International Journal of Fatigue 162 (2022) 106903.

[83] P. Carrion, F. Sausto, N. Shamsaei, S. Beretta, Multiaxial fatigue behavior and modelling of additive manufactured ti-6al-4v parts: The effects of layer orientation and surface defects, submitted to International Journal of Fatigue (2022).

Highlights

- Fatigue performances of AMed parts are strongly influenced by random parameters.
- To handle these random features a probabilistic fatigue postprocessor was developed.
- The main software's features were tested and compared to experimental data-points.
- The failure probability of AMed components was correctly estimated by the software.
- The software showed to be a suitable tool for the qualification of AMed parts.

Author declaration

We wish to confirm that there are no known conflicts of interest associated with this publication and there has been no significant financial support for this work that could have influenced its outcome.

We confirm that the manuscript has been read and approved by all named authors and that there are no other persons who satisfied the criteria for authorship but are not listed. We further confirm that the order of authors listed in the manuscript has been approved by all of us.

We confirm that we have given due consideration to the protection of intellectual property associated with this work and that there are no impediments to publication, including the timing of publication, with respect to intellectual property. In so doing we confirm that we have followed the regulations of our institutions concerning intellectual property.

We understand that the Corresponding Author is the sole contact for the Editorial process (including Editorial Manager and direct communications with the office). He is responsible for communicating with the other authors about progress, submissions of revisions and final approval of proofs. We confirm that we have provided a current, correct email address which is accessible by the Corresponding Author and which has been configured to accept email from stefano.beretta@polimi.it.

Signed by Stefano Beretta on the behalf of all authors: